Sensitivity of Dryline Convection Forecasts to Upstream Forecast Errors for Two Weakly Forced MPEX Cases

RYAN D. TORN

Department of Atmospheric and Environmental Sciences, University at Albany, State University of New York, Albany, New York

GLEN S. ROMINE

National Center for Atmospheric Research,[a] Boulder, Colorado

THOMAS J. GALARNEAU JR.

Department of Hydrology and Atmospheric Sciences, The University of Arizona, Tucson, Arizona

(Manuscript received 2 December 2016, in final form 13 February 2017)

ABSTRACT

The sensitivity of convective forecasts along the Texas dryline to upstream forecast fields at earlier lead times is evaluated for two consecutive days (27–28 May) characterized by no clear synoptic forcing for convection initiation (CI) during the 2013 Mesoscale Predictability Experiment (MPEX) by applying the ensemble-based sensitivity technique to convection-allowing WRF ensemble forecasts. For both cases, the members with stronger convection are characterized by higher water vapor just above the top of the boundary layer, which is associated with lower convective inhibition (CIN) at the time of CI. Forecast convection is sensitive to the lower-tropospheric water vapor and zonal wind at earlier lead times farther south along the dryline, such that increasing the water vapor and/or making the wind more easterly is associated with more convection. For 28 May, the water vapor along the dryline is also sensitive to the convection that occurs around 0600 UTC, which leads to cold pool–induced surface divergence that subsequently shifts the dryline north or south. Ensemble members that correctly have decreased convection in the Texas Panhandle on 28 May have more accurate forecasts of water vapor and meridional wind with respect to dropwindsondes in the sensitive region 9 h prior to CI compared to members with more extensive convection. Reducing the 0-h water vapor within the sensitive region can suppress convection in members with extensive convection; however, increasing the 0-h water vapor does not lead to more convection in members without convection.

1. Introduction

Errors in numerical weather prediction (NWP) model forecasts of severe mesoscale convective systems can originate from a number of different horizontal scales and processes. The classical view of forecast error growth is one where initial condition errors associated with the smallest scales grow upscale the fastest (e.g., Lorenz 1969; Zhang et al. 2003, 2006; Hohenegger and Schar 2007). More recent work suggests that error growth associated with convective systems is more complex, particularly in situations where convection is tied to larger horizontal-scale features, such as fronts, orography, or midtropospheric troughs. In these situations, the errors in the larger-scale features appear to introduce rapidly growing mesoscale perturbations, which in turn impact convective forecasts (e.g., Nuss and Miller 2001; Bei and Zhang 2007; Durran et al. 2013; Durran and Gingrich 2014; Durran and Weyn 2016). Nevertheless, it is of interest to understand how uncertainty in mesoscale fields and processes can impact subsequent convection forecasts, especially for cases that lack an obvious larger-scale feature that could focus convective initiation (CI); these cases are often more problematic for NWP models (e.g., Weisman et al. 2008).

One method by which the uncertainty associated with larger-scale features can impact CI is through the

---

[a] The National Center for Atmospheric Research is supported by the National Science Foundation.

Corresponding author e-mail: Ryan Torn, rtorn@albany.edu

DOI: 10.1175/MWR-D-16-0457.1

modification of the pre-CI environment. While there have been many studies on the role of kinematic (e.g., Coniglio et al. 2006; Richardson et al. 2007) and the temperature (e.g., McCaul et al. 2005; Kirkpatrick et al. 2009, 2011) uncertainty on convection forecast evolution, there have been relatively fewer studies highlighting the sensitivity to moisture, particularly above the boundary layer. While it is generally believed that having a drier midtroposphere leads to stronger downdrafts and surface outflow (e.g., Gilmore and Wicker 1998; James et al. 2006), other studies have demonstrated how midtropospheric humidity impacts more than just cold pool structure and speed. James and Markowski (2010) found that decreasing the humidity above the boundary layer decreases the intensity of convection, but has relatively little impact on the cold pool strength because the increased negative buoyancy is offset by the decreased hydrometeor concentration. Moreover, dry air has a larger impact on convection in low-CAPE environments compared to high-CAPE environments. Schumacher (2015) indicated strong sensitivity of elevated convection precipitation rates to the water vapor in the subcloud layer, such that lower water vapor in the subcloud layer makes it more difficult for subcloud layer parcels to be included in convective updrafts. Midtropospheric relative humidity appears to have a complicated impact on convective predictability, particularly when the relative humidity goes below a certain threshold, suggesting a nonlinear impact of relative humidity errors on convection forecasts (e.g., Wandishin et al. 2008).

One method of evaluating the sensitivity of convective forecasts to the initial conditions is to apply sensitivity analysis. There are numerous methods to estimate forecast sensitivities, including adjoint (e.g., Errico et al. 2003) and ensemble-based methods (e.g., Martin and Xue 2006; Melhauser and Zhang 2012; Bednarczyk and Ancell 2015; Torn and Romine 2015; Berman et al. 2017; Hill et al. 2016). Ensemble-based methods may be better posed for convective applications because they employ a set of nonlinear forecast trajectories to estimate sensitivities, rather than assuming linear forecast error growth (i.e., adjoints). Most of these studies have focused on situations where CI occurs in conjunction with well-defined synoptic-scale features. Moreover, many of these studies indicate that convective-oriented forecast metrics are sensitive to the position of these synoptic features because they modulate the position of boundaries and the characteristics of the preconvective environment and hence make CI more or less favorable. While Torn and Romine (2015) also observed significant sensitivity to upstream synoptic features that modified the thermodynamic environment, the sensitivity was greater to synoptic features that passed by the forecast metric of interest before CI takes place, suggesting that preconditioning of the environment early in the diurnal cycle had a longer-lasting impact on convective initiation.

The goal of this study is to understand how uncertainty in model forecast fields at earlier lead times impact subsequent convection forecasts along the Texas dryline under conditions characterized by weak synoptic-scale forcing for upward motion. The cases studied here took place during consecutive days of the Mesoscale Predictability Experiment (MPEX; Weisman et al. 2015) and were characterized by a similar synoptic setup, including no obvious upstream midtropospheric feature that might focus CI. One of the primary goals of MPEX was to collect observations that could be used to test the hypothesis that enhanced upstream observations during the early morning will provide a better representation of features that are not resolved by the current observation network, and hence improve convection forecasts during the afternoon over the high plains. Romine et al. (2016) suggest that assimilating this extra data had a mixed impact, which is at least partially due to how well the observations sampled the sensitive regions. Here, the ensemble-based sensitivity method applied to convection-permitting ensemble forecasts will be used to quantitatively compare how uncertainty in various upstream features and preconvective environments can impact subsequent convection forecasts along the Texas dryline. The sensitivities for these cases with weak forcing will be compared to the forecast sensitivities for strongly forced cases studied in Torn and Romine (2015) and Berman et al. (2017).

The remainder of the paper proceeds as follows. Section 2 describes the WRF forecasts and provides a brief summary of ensemble sensitivity analysis. A brief overview of 27–28 May is given in section 3, while the convective forecast sensitivities for these two days is described in sections 4 and 5, respectively. A summary and conclusions are given in section 6.

2. Forecast description

Forecast sensitivities are calculated from the same ensemble analysis and forecast system that was used in Torn and Romine (2015) and Berman et al. (2017), which were generated in real time during the MPEX field phase. A short summary of these forecasts is given here; the interested reader is directed to Schwartz et al. (2015) for a complete description of the system outlined below. Ensemble analyses are produced from a 50-member ensemble data assimilation system every 6 h starting

1 May–15 June 2013 on a 15-km horizontal grid-spacing domain that spans the continental United States [see Fig. 1 of Schwartz et al. (2015) for the exact dimensions]. Observations from rawinsondes, METAR, marine, aircraft meteorological data reports (AMDAR), atmospheric motion vectors (AMV; Velden et al. 2005), and Global Positioning System radio occultation observations (Kursinski et al. 1997) are assimilated using the Data Assimilation Research Testbed (DART; Anderson et al. 2009), which is an implementation of the ensemble adjustment Kalman filter (EAKF; Anderson 2001). The interested reader is directed to Table 3 of Romine et al. (2013) for a list of observation types that were assimilated from each platform and the observation error sources.

Both the data assimilation system and ensemble forecasts employ version 3.3.1 of the Advanced Research version of the Weather Research and Forecasting Model (ARW-WRF; Skamarock et al. 2008) with the following physics packages: Thompson microphysics (Thompson et al. 2008), Mellor–Yamada–Janjić (MYJ) planetary boundary layer (Mellor and Yamada 1982; Janjić 1994, 2001), Noah land surface model (Ek et al. 2003), Rapid Radiative Transfer Model (RRTM) longwave and shortwave radiation (Mlawer et al. 1997; Iacono et al. 2008) with ozone and aerosol climatologies (Tegen et al. 1997), and the Tiedtke cumulus parameterization (Tiedtke 1989; Zhang et al. 2011) and positive definite moisture advection (Skamarock and Weisman 2009). Ensemble lateral boundary conditions are taken from 6-h Global Forecast System (GFS) forecasts valid at the appropriate time with perturbations taken from the WRFDA-3DVAR (Barker et al. 2012) system via the fixed covariance perturbation (FCP) technique of Torn et al. (2006).

At 0000 UTC 27 and 28 May 2013, 50-member two-way nested ensemble forecasts are generated for the 15-km horizontal grid spacing outer domain and a 3-km horizontal grid spacing inner domain [see Fig. 1 of Schwartz et al. (2015) for the location of the 3-km domain]. Initial conditions for the 3-km domain are obtained by downscaling from the 15-km analysis domain. The 3-km domain uses the same physics packages as the 15-km domain, except that the 3-km domain does not employ a cumulus parameterization. Lateral boundary conditions for the 15-km domain are taken from the corresponding-time GFS forecast, with lateral boundary condition perturbations generated using the same FCP procedure employed for the data assimilation system.

Throughout this study, the sensitivity of forecast metrics on model state variables at earlier lead times is evaluated via the ensemble-based sensitivity technique. In particular, the sensitivity of a forecast metric J to the ith model state variable at some earlier time (x_i) is evaluated from a M member ensemble via

$$\frac{\partial J}{\partial x_i} = \frac{\mathrm{cov}(\mathbf{J}, \mathbf{x}_i)}{\mathrm{var}(\mathbf{x}_i)}, \qquad (1)$$

where $\mathbf{J}$ and $\mathbf{x}_i$ are $1 \times M$ ensemble estimates of the respective quantities computed from the forecast ensemble, cov denotes the covariance, and var denotes the variance. Similar to previous studies, x_i is normalized by the ensemble standard deviation, which allows for a quantitative comparison between fields that have different intrinsic variability and units. Statistical significance of the sensitivity values is tested by evaluating whether the absolute value of the regression coefficient is greater than the 95% confidence bounds, which means that the null hypothesis of no relationship between the metric and analysis state variable can be rejected (e.g., Torn and Hakim 2008).

3. Overview

The two days used in this study were characterized by a conditionally favorable environment for CI along the Texas dryline; however, there were no obvious synoptic forcings that would otherwise focus the convection. At 0000 UTC 27 May 2013, the surface is characterized by a strong north–south-oriented θ_e gradient indicative of a dryline located along the Texas–New Mexico border that separates the relatively moist air mass to the east from drier air to the west (Fig. 1a). Moreover, the 10-m winds are southeasterly throughout southern Texas to the east of the dryline, while the winds are more southwesterly to the west of the dryline. The 500-hPa flow is characterized by a broad midlatitude trough axis along the West Coast of the United States, with mainly westerly flow over Texas (Fig. 1b). Over the next 12 h, the dryline exhibits the typical diurnally driven westward motion while the upper-tropospheric flow remains qualitatively similar (Figs. 1c,d). Throughout the day on 27 May, the dryline moves eastward through Texas (Fig. 1e). By 0000 UTC, convection breaks out just to the east of the Texas portion of the dryline (Figs. 2a,d) due to the combination of relatively warm surface temperatures and high humidity that lead to a significant reduction in surface-based convective inhibition (CIN; not shown). In the midtroposphere, west Texas remains along the anticyclonic shear side of an upper-level jet streak along the Arizona–New Mexico border (Fig. 1f). Moreover, this analysis time is not characterized by any obvious midtropospheric features, or regions of enhanced convergence along the dryline that would help to focus convection, which might be expected to make

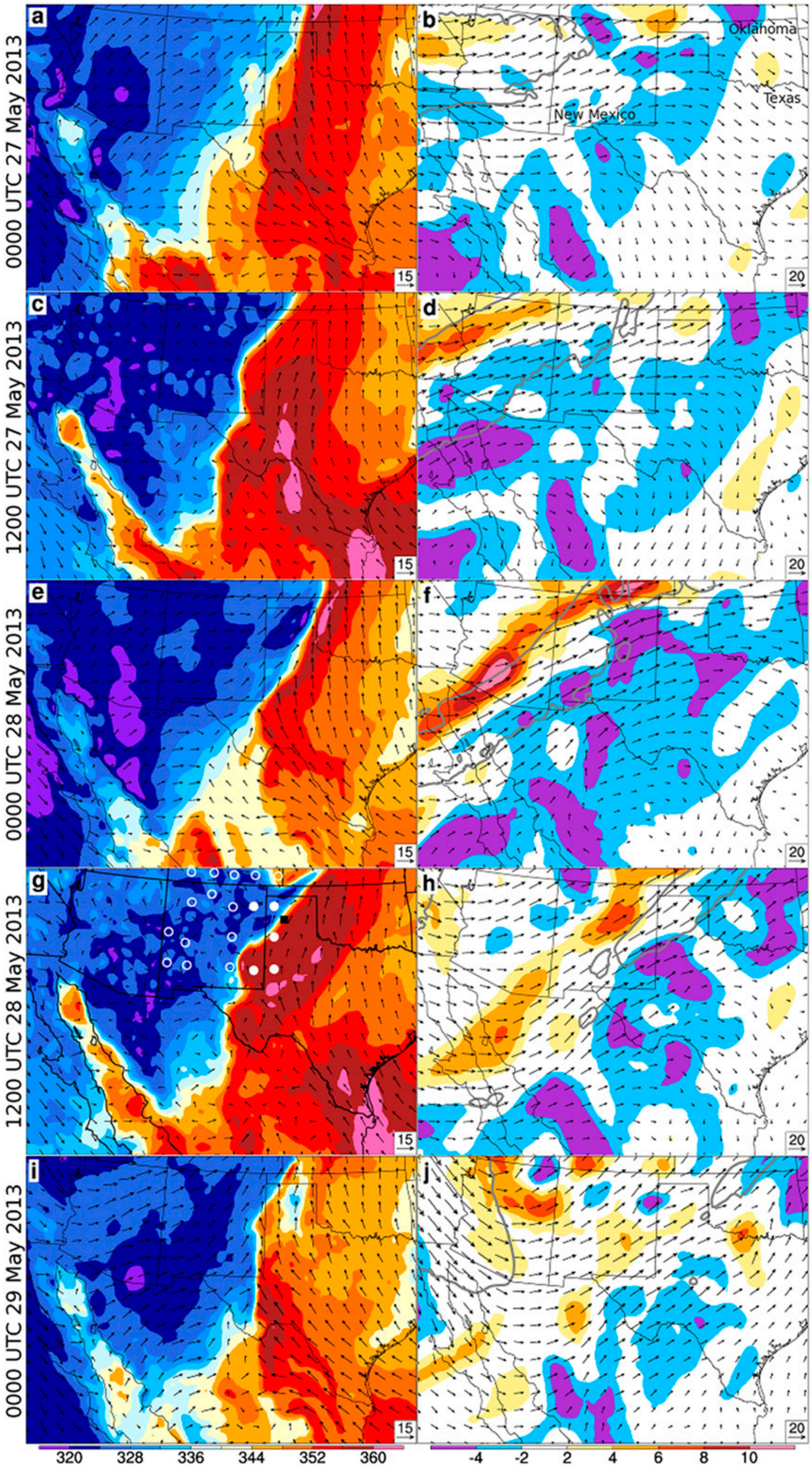

FIG. 1. (left) WRF-DART analysis of model-level 1 ($\sigma = 0.997$) equivalent potential temperature (color shading, K) and winds (vectors with reference vector at the bottom right of each panel, $m\,s^{-1}$) valid (a) 0000 UTC 27 May, (c) 1200 UTC 27 May, (e) 0000 UTC 28 May, (g) 1200 UTC 28 May, and (i) 0000 UTC 29 May 2013. (right) The 500-hPa relative vorticity (color shading, $\times 10^5\,s^{-1}$), winds (vectors, $m\,s^{-1}$), and the $30\,m\,s^{-1}$ isotach (gray) on the 300-hPa surface at the times corresponding to the left panels. In (g), the white dots denote the position of the sensitive MPEX dropwindsondes, other dropwindsondes are denoted by white circles, and the black square indicates Amarillo, TX.

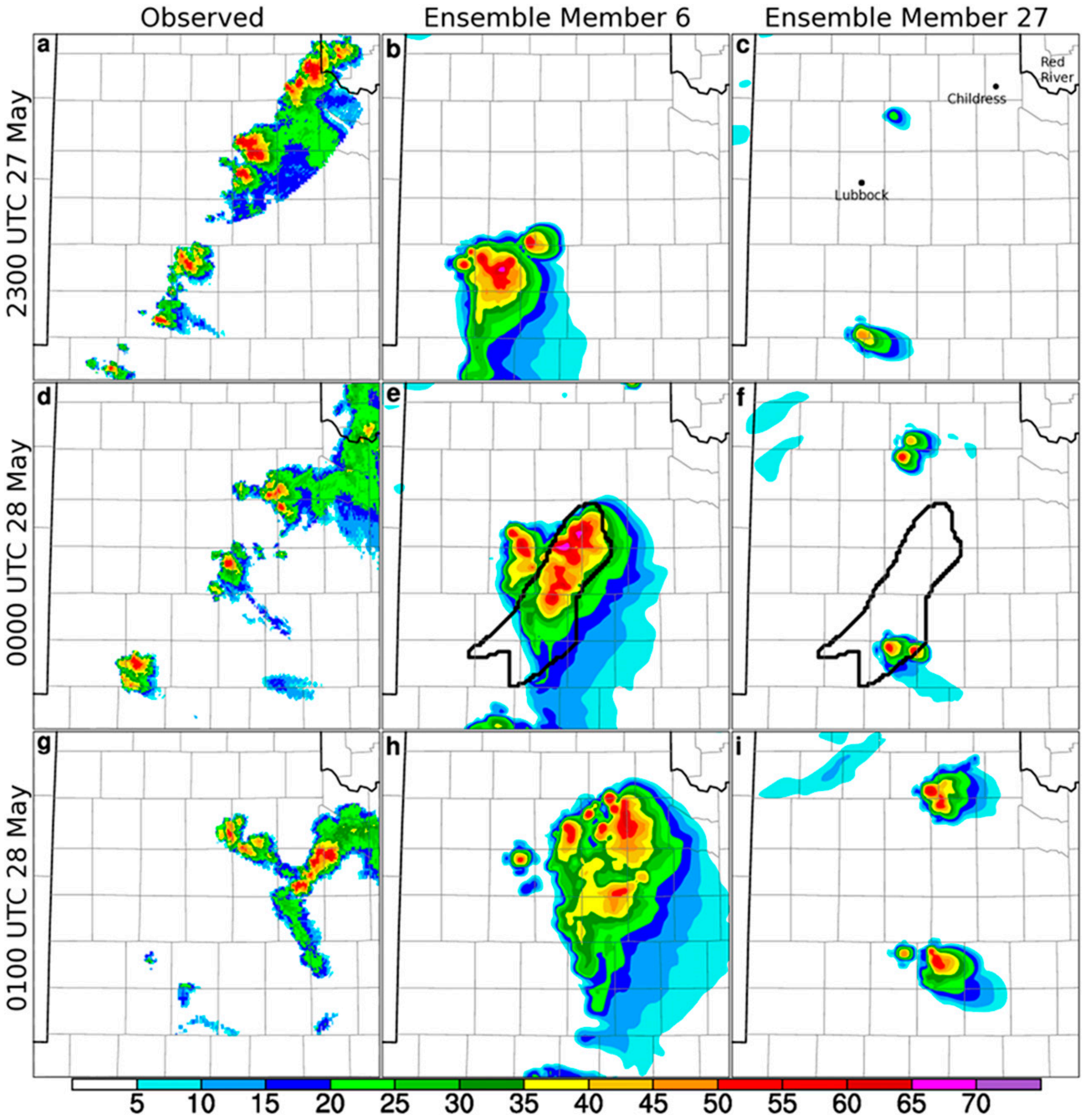

FIG. 2. (a) WSR-88D radar reflectivity at 2300 UTC 27 May 2013. The 23-h simulated column-maximum radar reflectivity forecast for ensemble members (b) 6 and (c) 27 initialized at 0000 UTC 27 May 2013. (d)–(f) As in (a)–(c), but valid at 0000 UTC 28 May 2013. The outlined area in (e) and (f) denote the forecast metric region used in the sensitivity calculations. (g)–(i) As in (a)–(c), but valid at 0100 UTC 28 May 2013.

this a more difficult convective forecast (discussed later). Nevertheless, isolated supercells eventually formed along the dryline in the afternoon (Fig. 2g), which resulted in multiple reports of hail exceeding 8 cm in diameter in Childress County, Texas (see the National Climatic Data Center storm event database maintained online at www.ncdc.noaa.gov/stormevents).

A similar pattern of dryline retreat and advance in a nondescript synoptic environment was repeated on 28 May, though convection was longer lasting farther to the north in the Texas Panhandle during the afternoon of 28 May. Similar to the day before, the dryline moves westward into southeast New Mexico between 0000 and 1200 UTC (Fig. 1g). Farther to the north, a southwest–northeast-oriented axis of drier air forms over the Texas and Oklahoma Panhandle and into southwestern Kansas associated with a lee cyclone that forms over Colorado. Beyond 1200 UTC, this lee cyclone leads to more southeasterly flow through much of Texas, raising the surface dewpoints and reducing the surface-based CIN to near zero by 1800 UTC at Amarillo, Texas (not shown). Similar to the day before, the upper levels continue to have broad southwesterly flow with little evidence of shortwave features that might help focus convection over the Texas and Oklahoma Panhandle (Figs. 1h,j). Convection initiates along the dryline starting at 2000 UTC (Figs. 3a,d,g), leading to numerous tornado, hail, and wind reports along the Texas–New Mexico border, as well as in the Oklahoma Panhandle (see the National Climatic Data Center storm event database maintained online at www.ncdc.noaa.gov/stormevents).

4. 27 May

Convection on 27 May was mainly isolated along the west Texas dryline, while WRF ensemble forecasts initialized at 0000 UTC are characterized by varied degrees of success in simulating the coverage and evolution. Between 2200 and 2300 UTC, isolated convection initiates along the dryline from the Red River southward (Fig. 2a); however, much of this convection was short lived as many of these cells decayed by 0000 UTC (Fig. 2d), though a small line did eventually form near Childress by 0100 UTC (Fig. 2g). Some ensemble members, such as member 6, have a cluster of cells that initiate near Lubbock, Texas, at 2200 UTC (Fig. 2b) and that move poleward along the dryline as a MCS, due to the merger of outflows and proximity of convective cells, before becoming more disorganized as it neared Oklahoma at 0100 UTC (Figs. 2e,h). By contrast, others including member 27 feature isolated, discrete cells, which remain short lived and unable to organize into an MCS (Figs. 2c,f,i).

Given the variety of convective forecasts along the dryline, it is of interest to evaluate why some members have more extensive convection in this area, while others do not. This approach requires a forecast metric that measures convective strength, yet has minimal influence from nonconvective processes (i.e., stratiform precipitation). As a consequence, this study employs the maximum vertical kinetic energy [$(1/2)w_{\max}^2$, where $w_{\max}$ is the maximum vertical motion in a column) forecast metric averaged over a geographic area and time period (hereafter J_{VKE}).[1] This metric has been used in previous studies (e.g., Berman et al. 2017) and unlike precipitation or reflectivity-based metrics, which have been used in other sensitivity studies (e.g., Bednarczyk and Ancell 2015; Torn and Romine 2015; Hill et al. 2016), it is relatively straightforward to separate convection from extensive stratiform precipitation. Moreover, the time period of the greatest variability in this metric occurs between 22 and 25 h (2200–0100 UTC); therefore, this time period is used in the metric calculation.

Rather than prescribing a rectangular forecast metric area that may or may not efficiently enclose the geographic region of greatest variability in convection, an objective algorithm is employed to define the geographic area that is based on the 2D distribution of the standard deviation of the maximum vertical kinetic energy over this time period. First, each member's 2D distribution of maximum vertical kinetic energy is spatially smoothed using a Gaussian kernel with a 15-km *e*-folding distance. Next, the standard deviation of the smoothed maximum vertical kinetic energy is computed at each horizontal grid point. The smoothing is needed because of the discrete nature of the maximum vertical kinetic energy (i.e., mainly tied to updrafts). If smoothing is not used, the standard deviation tends to be large where individual ensemble members have strong updrafts due to the relatively small number of ensemble members used here. A much larger ensemble would likely not require this smoothing step. The metric area is defined as all of the contiguous grid points that have a maximum vertical kinetic energy standard deviation that is greater than a certain percentage of the maximum grid point value. For this forecast, the minimum threshold is $16\,\mathrm{m^2\,s^{-2}}$, which is equivalent to 65% of the maximum standard deviation.[2] This metric mainly measures the geospatial extent of active convection during this time period. It is worth noting that the sensitivity results are relatively insensitive to the time period (i.e., computing the forecast metric over longer periods of time) and small changes to the geospatial area (not shown).

One hypothesis for the different convection evolution within the ensemble is that some members have a more conducive preconvective environment. This hypothesis is evaluated by comparing the composite vertical profiles of various thermodynamic quantities within the forecast metric area for the 10 members with the largest J_{VKE} and the 10 members with the smallest J_{VKE}. The statistical significance of the composite differences is evaluated via a bootstrap resampling

---

[1] This quantity is taken from the WRF output maximum vertical motion at each horizontal grid point each hour.

[2] This value is entirely arbitrary. It was chosen because it encloses the region of greatest uncertainty; see Fig. 2e for geospatial extent.

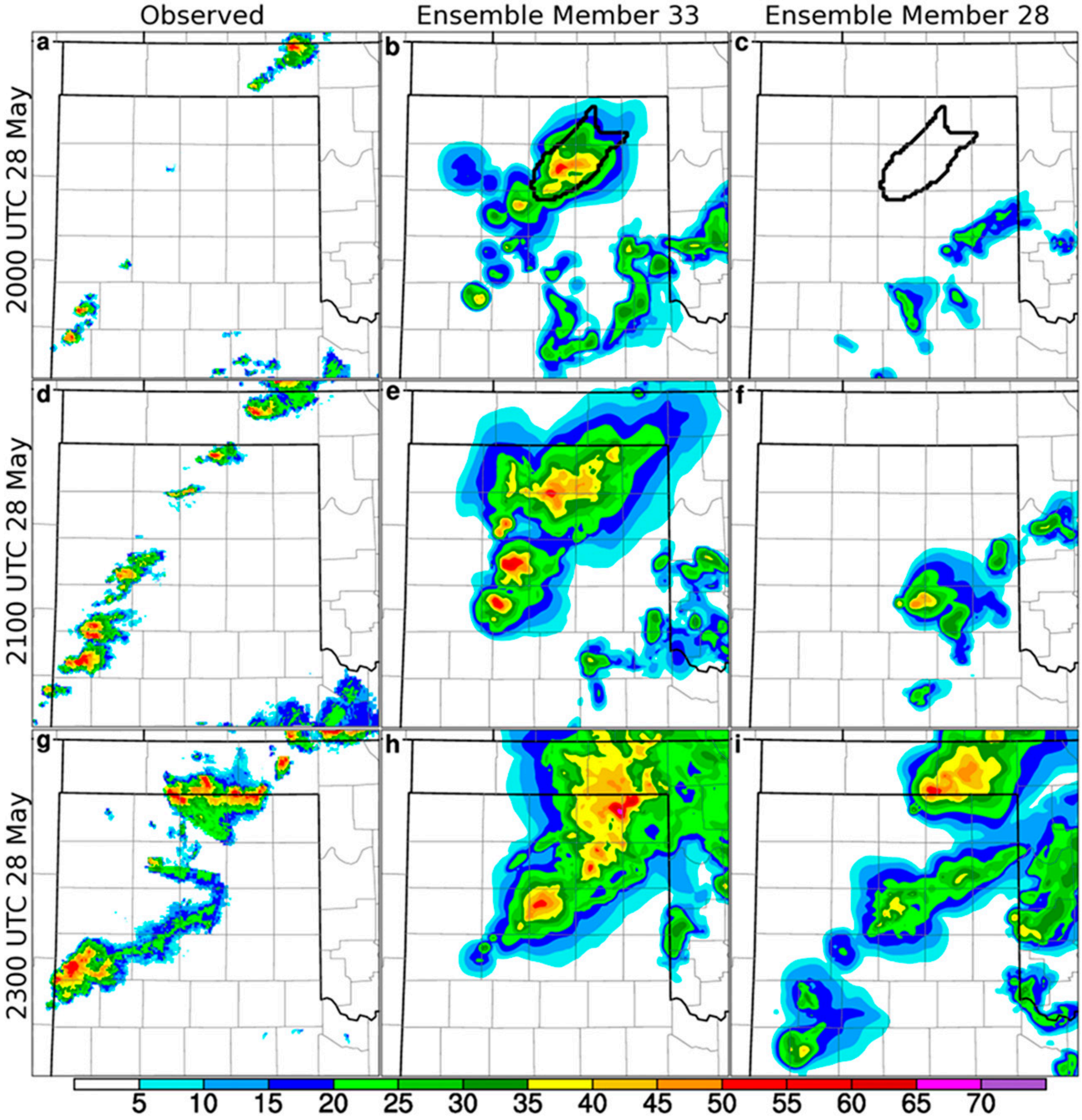

FIG. 3. As in Fig. 2, but for 2000 UTC 28 May 2013. The 20-h simulated column-maximum radar reflectivity forecast for ensemble members (b) 33 and (c) 28 initialized at 0000 UTC 28 May 2013. The outlined area in (b) and (c) denote the forecast metric region used in the sensitivity calculations. (d)–(f) As in (a)–(c), but valid at 2100 UTC 28 May 2013. (g)–(i) As in (a)–(c), but valid at 2300 UTC 28 May 2013.

method described in Torn and Romine (2015), which involves randomly selecting two sets of 10 ensemble members and evaluating the probability that the difference between the large and small J_{VKE} is obtained by random chance.

Figure 4 indicates that members associated with greater convection in the metric area are characterized by a more thermodynamically favorable lower troposphere just prior to CI (2100 UTC). In particular, the members with large J_{VKE} have significantly higher θ_e from the surface to 500 hPa (Fig. 4a), with the largest differences (5.3 K) at 810 hPa, which is within the large vertical gradient in the ensemble-mean θ_e above the ensemble-mean boundary layer. Separating θ_e into the

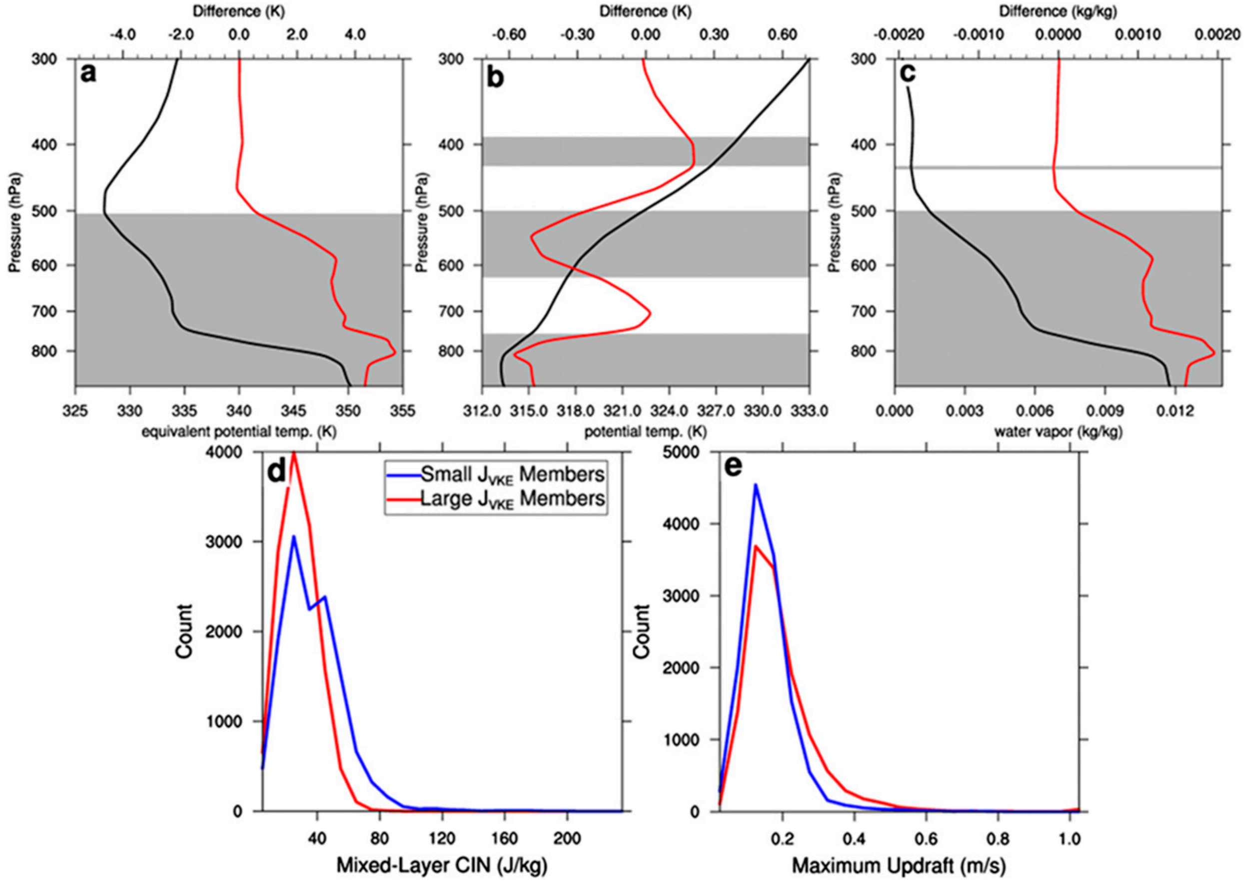

FIG. 4. Vertical profile of the difference in the 21-h (a) equivalent potential temperature, (b) potential temperature, and (c) water vapor mixing ratio averaged over the metric area shown in Fig. 2e between the 10 members with largest J_{VKE} and the 10 members with the smallest J_{VKE} as a function of pressure (red line) initialized at 0000 UTC 27 May 2013. The shaded regions indicate vertical levels where the difference is statistically significant at the 95% confidence level. The black line gives the ensemble-mean profile (K, K, and kg kg^{-1}, respectively). Histograms of the 21-h (d) CIN and (e) column-maximum upward vertical motion averaged over the forecast metric region for the 10 members with the largest J_{VKE} (red) and the 10 members with the smallest J_{VKE} (blue).

potential temperature (Fig. 4b) and water vapor components (Fig. 4c) indicates that the higher θ_e in the large J_{VKE} members is mainly due to water vapor. While the large J_{VKE} members have statistically larger water vapor than the small J_{VKE} members from the surface to 500 hPa (maximum difference of 0.002 kg kg^{-1} at 800 hPa), the large J_{VKE} members are actually up to 0.5 K colder below 800 hPa than the low J_{VKE} members, which will yield a colder and more moist boundary layer, Moreover, the boundary layer depths of these two groups of members are similar (not shown).

These thermodynamic differences also manifest as different amounts of convective inhibition and vertical motion at the same time. While the large J_{VKE} members have on average 30 J kg^{-1} lower mixed-layer CIN (MLCIN) at 2100 UTC, histograms of this quantity for all grid points within the forecast metric region show quantitative differences in the distribution. While both the large and small J_{VKE} members peaked around 25 J kg^{-1}, the small J_{VKE} members have fewer grid points with a MLCIN at 25 J kg^{-1} and many more grid points with MLCIN above 50 J kg^{-1} (Fig. 4d). This difference in MLCIN translates into differences in column-maximum vertical motion, such that the small J_{VKE} members have few grid points above 0.3 m s^{-1} at this time, while the large J_{VKE} members have more (Fig. 4e).

The previous results suggest that an important discriminator between having large and small J_{VKE} is the lower-tropospheric water vapor; therefore, it is of interest to evaluate the sensitivity of J_{VKE} to the 750–850-hPa integrated water vapor (layer that is characterized by the largest difference between large and small J_{VKE}) at earlier lead times (Fig. 5). Given the proximity of this metric to the dryline and previous studies that demonstrate the sensitivity of convection forecasts to moisture boundary locations (e.g., Bednarczyk and Ancell 2015;

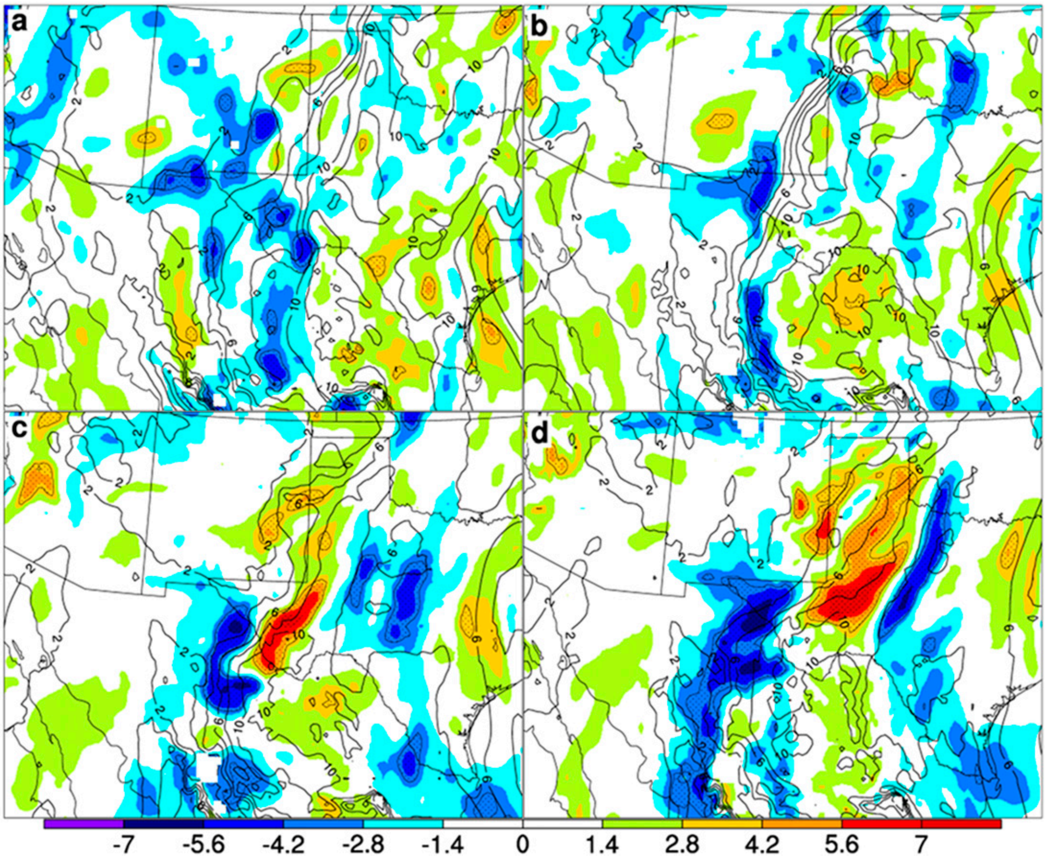

FIG. 5. Sensitivity of the 22–25-h maximum vertical kinetic energy averaged over the closed curve shown in Fig. 2e to the (a) 0-, (b) 6-, (c) 12-, and (d) 18-h 750–850-hPa integrated water vapor (color shading, $m^2 s^{-2}$) initialized at 0000 UTC 27 May 2013. Stippled regions indicate where the sensitivity is statistically significant at the 95% confidence level. Contours are the ensemble mean at the respective time ($kg\,m^{-2}$).

Torn and Romine 2015; Berman et al. 2017; Hill et al. 2016), one hypothesis is that J_{VKE} is sensitive to the dryline position. At 1800 UTC (3 h prior to CI), the sensitivity of J_{VKE} to 750–850-hPa water vapor exhibits positive values along the west Texas dryline (up to $8.0\,m^2 s^{-2}$ per standard deviation) and negative sensitivity values farther south along the dryline along the Texas–Mexico border and into Mexico (up to $-7.0\,m^2 s^{-2}$ per standard deviation; Fig. 5d). This pattern of sensitivity suggests that greater J_{VKE} occurs when the dryline is farther to the west through west Texas, but is farther east to its south into Mexico. As will be shown later, the eastern and western dryline position perturbations are likely related to each other. Proceeding backward in time, the sensitive region shifts farther south along the dryline over far west Texas at 1200 UTC ($7.2\,m^2 s^{-2}$ per standard deviation; Fig. 5c). By contrast, J_{VKE} does not appear to have a statistically significant sensitivity to the 750–850-hPa water vapor at 0600 UTC or earlier (Figs. 5a,b). There are multiple reasons for why this result might be obtained, including that the location of the dryline around 0000 UTC has little memory of the position more than 12 h in the past due to other processes (i.e., advection, radiative cooling, turbulent mixing), and/or that the non-Gaussian ensemble distribution of J_{VKE}, which could make it harder to determine a linear relationship between the metric and forecast fields before 1200 UTC due to the smaller ensemble variance at earlier times. Finally, another possibility is that locations upstream of far west Texas (i.e., over Mexico) have a surface pressure below 850 hPa; therefore, the 750–850-hPa layer is likely to be within the PBL and thus would be strongly influenced by the PBL parameterization.

One method to potentially address the lack of sensitivity to the 750–850-hPa water vapor at earlier lead times is to compute the sensitivity of metrics related to the preconvective environment within the J_{VKE} region. Given that the pre-CI water vapor difference between large and small J_{VKE} members is maximized between

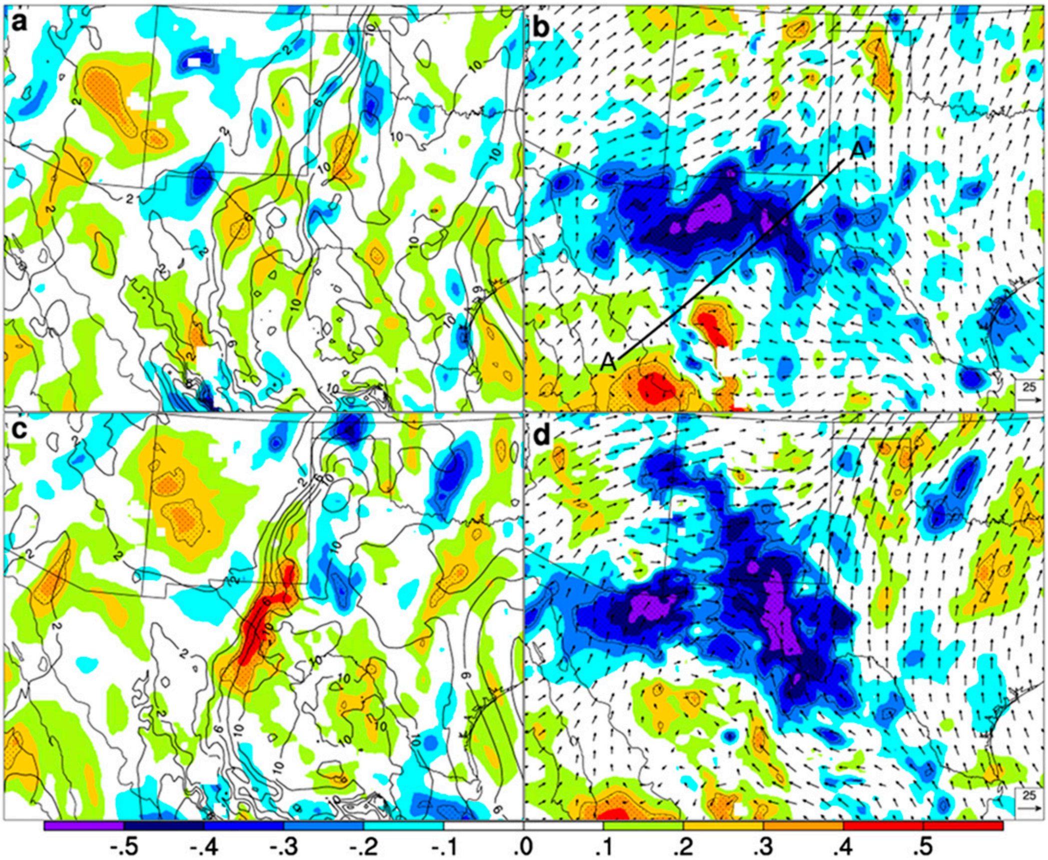

FIG. 6. Sensitivity of the 21-h 750–850-hPa integrated water vapor averaged over the metric region shown in Fig. 2e to the 0-h 750–850-hPa (a) integrated water vapor and (b) zonal wind (color shading, kg m^{-2}) initialized at 0000 UTC 27 May 2013. Stippled regions indicate where the sensitivity is statistically significant at the 95% confidence level. The contours and vectors are the ensemble-mean values (kg m^{-2} and m s^{-1}, respectively). The black line in (b) denotes the location of the cross section for Fig. 7. (c),(d) As in (a),(b), but for the 6-h forecast.

750 and 850 hPa at 2100 UTC, the sensitivity of this metric (hereafter J_{q_v}) to various fields at earlier times is also computed. In essence, this calculation can be used to diagnose how processes at earlier times can modulate the evolution of the 750–850-hPa water vapor within the metric region, which in turn is expected to influence J_{VKE}. Note that the correlation between J_{VKE} and J_{q_v} is 0.81; therefore, these two metrics are strongly related to one another.

Indeed, computing the sensitivity of J_{q_v} to lower-tropospheric fields indicates clearer areas of high sensitivity that are traceable to distinct locations at 0 h. Figure 6a indicates that J_{q_v} appears to exhibit minimal sensitivity to the 0000 UTC (0 h) 750–850-hPa water vapor along the dryline; however, by 0600 UTC, the sensitivity is maximized (0.5 kg m^{-2} per standard deviation) where the dryline intersects the Texas–Mexico border (Fig. 6c), indicating that J_{q_v} is increased by having the dryline to the west (not shown), which is similar to the sensitivity of J_{VKE} to the 750–850-hPa integrated water vapor at later lead times. Moreover, J_{q_v} shows clear negative sensitivity to the 0- and 6-h 750–850-hPa zonal component of the wind over northern Mexico, such that decreasing the zonal component of the wind by one standard deviation is associated with up to a 0.6 kg m^{-2} increase in integrated water vapor in the metric region (Figs. 6b,d). Moreover, the zonal wind sensitivity extends across both sides of the dryline, suggesting that J_{q_v} is increased by making the zonal component of the wind more easterly, which in turn leads to greater advection of moist lower-tropospheric air from east to west, hence moving the dryline in that direction (not shown).

The aforementioned wind sensitivity appears to be tied to the position of a weak lower-tropospheric PV anomaly moving northeast along the anticyclonic side of the subtropical jet. Figure 7 provides a cross section of the sensitivity to the 0000 UTC wind normal to the cross section and PV. The sensitivity to the wind normal to the cross section is mainly confined below 600 hPa to the

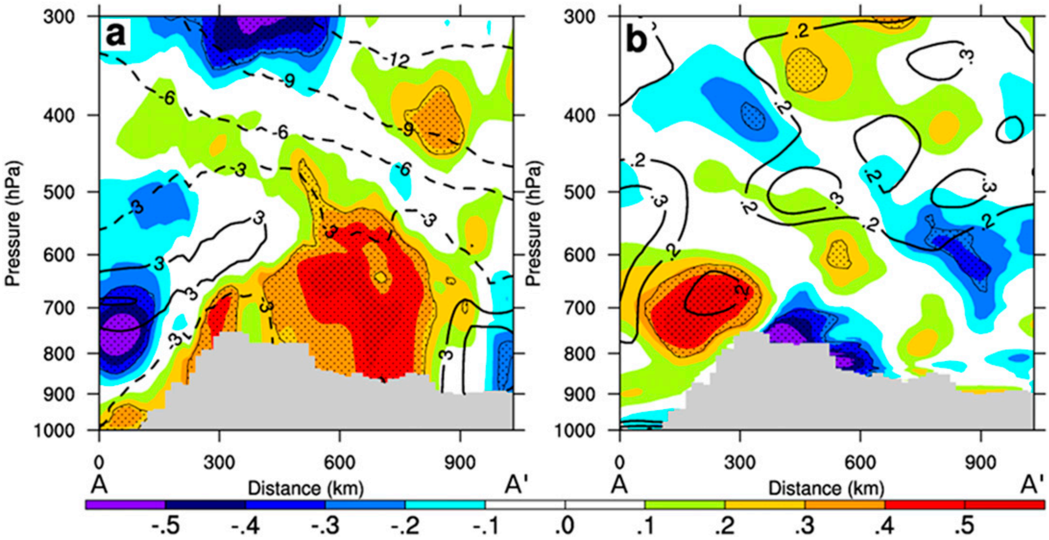

FIG. 7. Sensitivity of the 21-h 750–850-hPa integrated water vapor averaged over the metric region shown in Fig. 2e to the 0-h (a) wind normal to the cross section (positive indicates into the cross section) and (b) potential vorticity along the cross section shown in Fig. 6b (color shading, kg m^{-2}) initialized at 0000 UTC 27 May 2013. Stippled regions indicate where the sensitivity is statistically significant at the 95% confidence level. The contours are the ensemble-mean fields [m s^{-1} and PVU in (a) and (b), respectively].

east of the Sierra Madre Occidental range (high point in the topography near 300 km), which is within a region characterized by a near-zero ensemble-mean normal wind (Fig. 7a). This normal wind sensitivity appears to be associated with a positive PV sensitivity maximum at 700 hPa on the west side of Sierra Madre Occidental (Fig. 7b), which subsequently moves northeast over the forecast (not shown). This result suggests that convection variability on this day along the dryline is originally tied to uncertainty in the lower-tropospheric winds to the south of the Rio Grande Valley in Mexico. These perturbation easterly winds need time to advect higher water vapor westward, which would explain why the sensitivity to the 750–850-hPa moisture is present at 0600 UTC, but not 0000 UTC. Moreover, the westerly winds on the south side of this anomaly act to advect the dryline to the east farther south, thus explaining the negative water vapor sensitivity to the south of the region of positive water vapor sensitivities described earlier.

5. 28 May

Similar to 27 May, WRF ensemble forecasts on 28 May were characterized by varied degrees of convective extent and vigor. At 2000 UTC, convection initiated along the dryline near the Texas–New Mexico border, as well as in the Oklahoma Panhandle (Fig. 3a). One hour later, additional cells attempt to initiate close to the original CI locations, though much of the Texas Panhandle remains convection free (Fig. 3d). By 2300 UTC, the Texas–New Mexico convection remains nearly stationary, while some of the cells along the Texas–Oklahoma border begin to consolidate and move southward (Fig. 3g). WRF ensemble forecasts initialized at 0000 UTC are characterized by varied degrees of being able to simulate the distribution of convection in the Texas Panhandle, particularly in the region where little convection was observed during this period. Some members, including member 33, have a large convective area within the region where no convection was observed. These cells eventually consolidate into a north–south-oriented convective line as the cold pools of each of the individual cells merge together (Figs. 3b,e,h). By contrast, member 28 has little convection within the Texas Panhandle throughout the period, captures the southward-moving cells out of the Oklahoma Panhandle, but misses the Texas–New Mexico border supercells (Figs. 3c,f,i). During this period (1900–2100 UTC), the region of largest variability in maximum vertical kinetic energy during the CI period is in the Texas Panhandle; therefore, J_{VKE} is evaluated over this region, which was determined using the algorithm outlined in the previous section (encompasses all grid points with maximum vertical kinetic energy exceeding 10 m^2 s^{-2}). It is worth noting that geospatially larger metric areas that include both the Texas and Oklahoma Panhandles and southwest Kansas indicate qualitatively similar results (not shown).

Convection forecasts during this day exhibit similar thermodynamic field differences as the day before. Figure 8a indicates that the members with the large

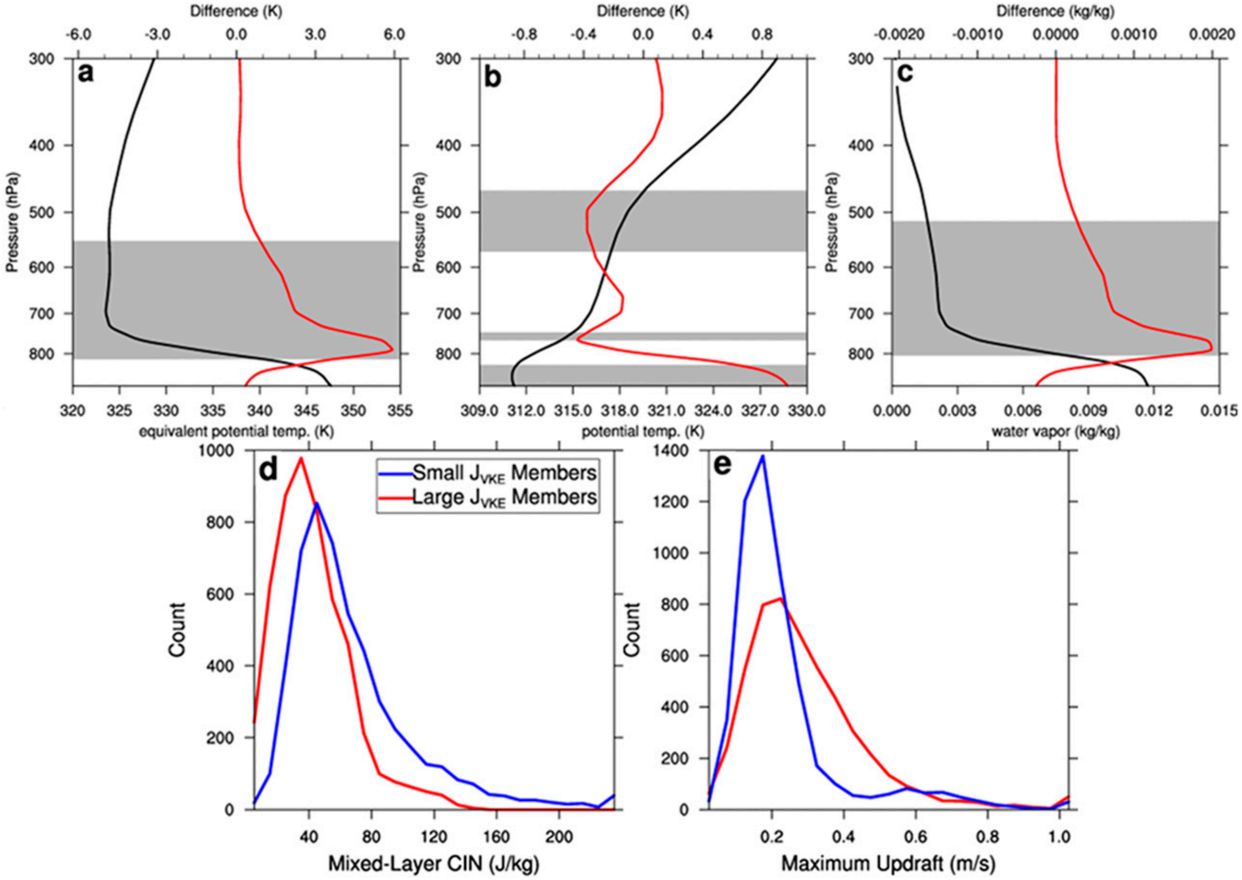

FIG. 8. As in Fig. 4, but for the difference in the 18-h values averaged over the metric area shown in Fig. 3b as a function of pressure (red line) initialized at 0000 UTC 28 May 2013. Histograms are of the 18-h CIN and maximum upward vertical motion.

J_{VKE} are characterized by statistically greater θ_e between 550 and 800 hPa compared to the small J_{VKE} members at 1800 UTC. The differences are maximized at 800 hPa (6 K), which is within the large vertical gradient in ensemble-mean θ_e above the ensemble-mean boundary layer. Moreover, the θ_e differences are primarily related to water vapor, as the temperature differences are generally small and statistically insignificant (Fig. 8b), while the water vapor mixing ratio differences are statistically significant through the same layer as the statistically significant θ_e differences, which are maximized at 800 hPa (2 g kg^{-1}), but near zero within the boundary layer itself (Fig. 8c). Moreover, the large J_{VKE} exhibit some evidence of slightly deeper boundary layers and lower static stability between 750 and 800 hPa, which allows for deeper mixing of heat and moisture. The large J_{VKE} members have a distribution of MLCIN that is peaked at 35 J kg^{-1}, with few points above 80 J kg^{-1} (Fig. 8d). By contrast, the small J_{VKE} members are peaked 10 J kg^{-1} higher and there are a significant number of points with MLCIN greater than 80 J kg^{-1}, which would make CI less likely. Maximum vertical motion differences are consistent, such that the large J_{VKE} members have many grid points with maximum vertical motion above 0.3 m s^{-1}, while the small J_{VKE} members do not (Fig. 8e). Overall, these differences suggest that the combination of lower stability at the top of the boundary layer and moisture above the boundary layer make it easier for CI to take place for the large CI members.

Similar to the 27 May forecasts, J_{VKE} is sensitive to the evolution of the lower-tropospheric water vapor along the dryline prior to CI. Figure 9 shows the sensitivity to the 700–800-hPa integrated water vapor at various lead times up to CI. At 1800 UTC, J_{VKE} is sensitive to the integrated water vapor along the dryline through the Texas Panhandle just upstream of the metric region (maximum: 7 m^2 s^{-2} per standard deviation; Fig. 9d). Six hours earlier, this sensitive region is farther upstream along the water vapor gradient in the Texas–New Mexico border (maximum: 8.0 m^2 s^{-2} per standard deviation; Fig. 9c), suggesting that the sensitive region is being advected poleward by the lower-tropospheric southwesterly winds. Similar to the sensitivity on 27 May,

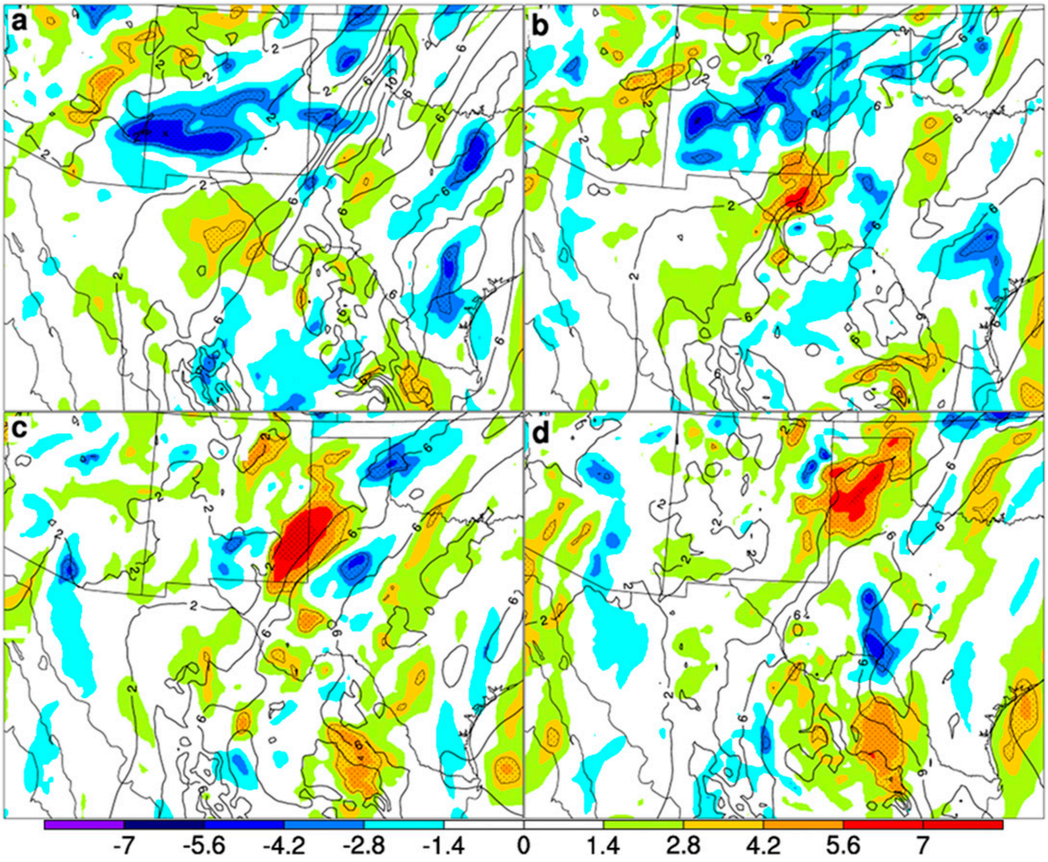

FIG. 9. As in Fig. 5, but for 19–21-h values averaged over the box shown in Fig. 3b to the 700–800-hPa integrated water vapor (initialized at 0000 UTC 28 May 2013).

it becomes more difficult to identify the sensitive region prior to 1200 UTC. While there is a relatively small sensitive region over far west Texas at 0600 UTC (Fig. 9b), there appears to be few places where the sensitivity of J_{VKE} to the 0000 UTC water vapor is statistically significant (Fig. 9a).

The lack of sensitivity to the 0-h 700–800-hPa water vapor motivates looking at the sensitivity to the 1800 UTC water vapor within the J_{VKE} region (again denoted J_{q_v}). Figure 10a indicates that the 18-h 700–800-hPa integrated water vapor within the J_{VKE} region is most sensitive to the initial-time 700–800-hPa integrated vapor along the dryline location on the Texas–Mexico border (up to 0.52 kg m^{-2} per standard deviation), such that shifting the position of the dryline to the northwest in this region is associated with higher integrated vapor over the convective region of interest 18 h later. Taking a cross section normal to the dryline along the Texas–Mexico border indicates that J_{q_v} is sensitive to the water vapor along the ensemble-mean dryline up to roughly 500 hPa (Fig. 10b). In addition, J_{q_v} exhibits negative sensitivity to the wind parallel to the cross section to the east of the dryline, such that making the wind more southeasterly is associated with higher water vapor later in the forecast. This result is qualitatively consistent with the 27 May results, such that enhancing the 0-h easterly return flow along the dryline helps to move the dryline farther west, which leads to a more thermodynamically favorable environment in the area of interest during the subsequent diurnal heating period.

While it might seem like this case is a straightforward instance of where 0-h wind and water vapor perturbations advect poleward along the dryline into the forecast metric region, the evolution of ensemble perturbations is complicated by an area of elevated convection that initiates in Mexico around 0330 UTC and moves into far west Texas thereafter. At 0600 UTC, the composite radar image indicates a single cell (Fig. 11a); however, this region has insufficient radar coverage. Indeed, IR satellite images suggest that convective coverage was more extensive at this time (not shown). Some members of the ensemble (including member 4) have a slow-moving complex, while others are shifted south and are less extensive (Figs. 11b,c). The differences in convective

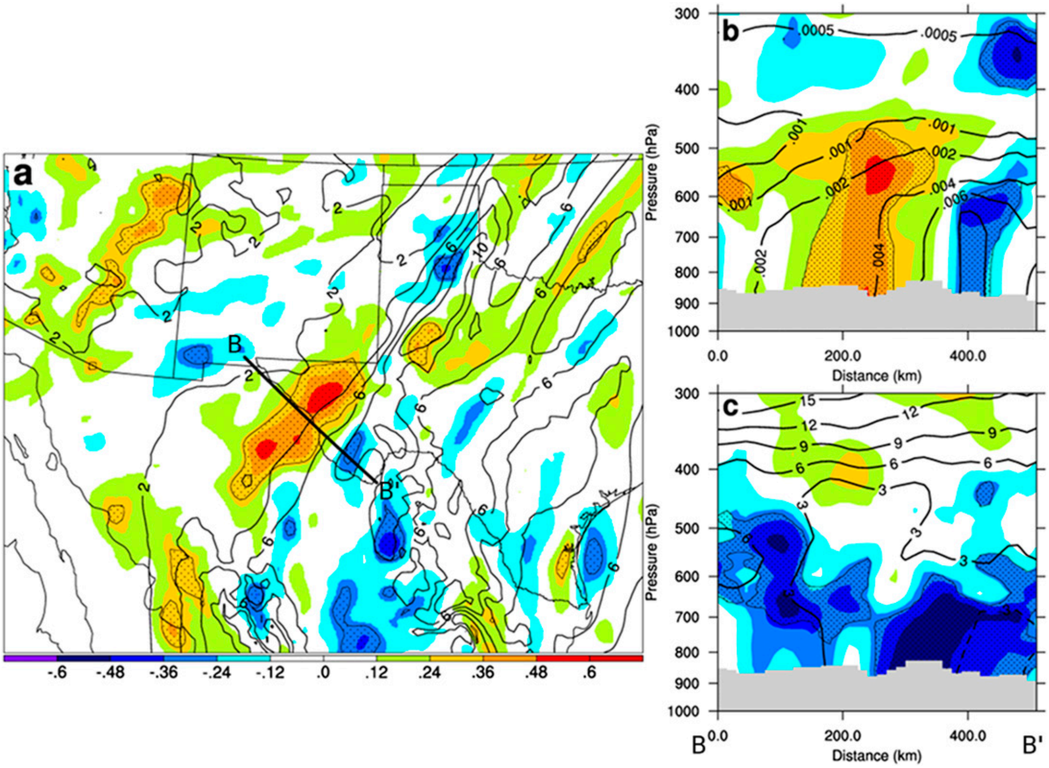

FIG. 10. (a) Sensitivity of the 18-h 700–800-hPa integrated water vapor averaged over the metric region shown in Fig. 3b to the (a) 0-h 700–800-hPa integrated water vapor (color shading, kg m^{-2}) initialized at 0000 UTC 28 May 2013. Stippled regions indicate where the sensitivity is statistically significant at the 95% confidence level. The contours are the ensemble-mean values (kg m^{-2}). (b),(c) Cross sections of the sensitivity to water vapor mixing ratio and wind parallel to the cross section along the line in (a) (positive values are directed from B to B′), respectively; contours denote the ensemble mean values (kg kg^{-1} and m s^{-1}, respectively).

extent within this region might be expected to produce different cold pool extents, which could also modify the location of the dryline and explain the lack of sensitivity of J_{VKE} to water vapor at earlier times. As a consequence, it is worthwhile to compute the sensitivity of the 4–7-h maximum vertical kinetic energy within the region outlined in Fig. 11b (region of maximum kinetic energy uncertainty) to the 0-h forecast fields to evaluate how this convection is impacted by uncertainty at earlier lead times and how this convection subsequently impacts the lower- to midtropospheric water vapor field near the dryline later in the day.

The west Texas convection is characterized by initial condition sensitivities that are qualitatively similar to the J_{q_v} sensitivities shown previously (Fig. 12). In particular, the west Texas J_{VKE} is sensitive to the 0-h 700–800-hPa integrated water vapor where the dryline intersects the Texas–Mexico border, such that increasing the water vapor, akin to shifting the dryline to the northwest, is associated with more intense convection a few hours later (Fig. 12a). In addition, the west Texas J_{VKE} is sensitive to the zonal wind just south of the Texas–Mexico border, such that a more easterly wind, which would lead to anomalous positive moisture advection and upslope flow, is associated with more convection. At 0600 UTC, which is roughly coincident with the timing of J_{VKE}, the sensitivity to the 700–800-hPa integrated water vapor is much smaller (2.5 m^2 s^{-2} per standard deviation), likely due to the fact that cold pools within the members with large J_{VKE} partially offset the higher 700–800-hPa integrated water vapor present at 0 h (Fig. 12c). By contrast, J_{VKE} remains sensitive to the zonal component of the wind on the eastern side of the dryline, such that the 0-h sensitive region has shifted north and is over far west Texas.

Beyond 0600 UTC, the result of having large or small J_{VKE} appears to have a significant impact on the subsequent wind and water vapor fields. Figure 12e shows the impact of J_{VKE} on the 12-h 700–800-hPa integrated moisture. The impact pattern is complex, with a positive impact along and to the east of the dryline along the Texas–Mexico border and a second maximum along the Texas–New Mexico border, which coincides with the positive sensitivity region for J_{VKE} shown previously

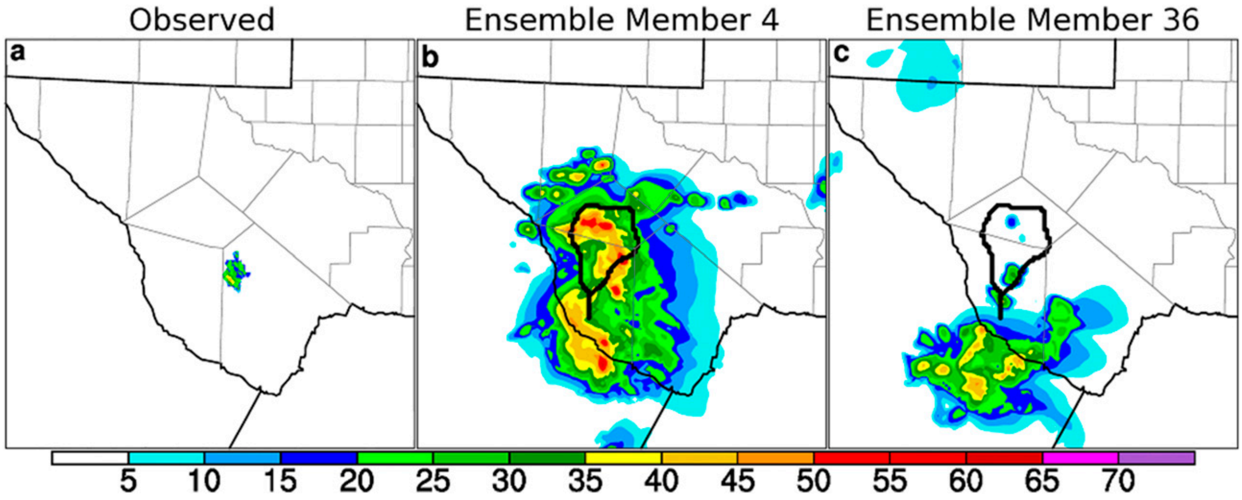

FIG. 11. (a) WSR-88D radar reflectivity at 0600 UTC 28 May 2013. (b),(c) The 6-h simulated radar reflectivity forecast for ensemble members 4 and 36, respectively, initialized at 0000 UTC 28 May 2013; the outlined area denotes the forecast metric region used in the sensitivity calculations.

(Fig. 9c). In addition, there is a region of negative impact in between these two regions of positive impact near Midland, Texas, which indicates that members with greater convection have lower θ_e in this region, likely reflecting the remnant cold pools from the earlier convection. Furthermore, higher J_{VKE} is associated with positive meridional wind along the Texas–New Mexico border and negative meridional wind along the Texas–Mexico border (Fig. 12f). These positive–negative wind impacts straddle the aforementioned negative water vapor impacts and suggest greater lower-tropospheric divergence centered on the remnant cold pool. Taking a north–south cross section through the region of maximum perturbation indicates the relatively shallow nature of the differences, such that higher west Texas J_{VKE} is associated with lower water vapor below 700 hPa in the middle of the cross section, which coincides with the remnant cold pool, but with positive values on either side (Fig. 13a). The positive water vapor values appear to be due to the lower-tropospheric perturbation meridional winds associated with the downdrafts and cold pool movement (Fig. 13b), which help advect the dryline to the north, and subsequently lead to a more moist environment in the Texas Panhandle later in the day (not shown).

Overall, this set of sensitivities suggest a complex set of circumstances that modulate the preconvective environment on this day. Increasing the 0-h easterly component of the wind through the Rio Grande Valley leads to greater upslope flow, which in turn helps destabilize the atmosphere in this area. The environment is relatively dry in this region; therefore, convection produces strong downdrafts, which appear 6 h into the forecast. The downdraft perturbation winds subsequently advect the dryline poleward along the Texas–New Mexico border, which is on the north side of the cold pool. In turn, this leads to greater midtropospheric moisture over the Texas Panhandle metric region later in the day on 28 May. Although it may be tempting to believe that the Texas Panhandle J_{VKE} is dictated by the west Texas J_{VKE} (the correlation coefficient between these two metrics is 0.64), it is likely that the covariability between these two metrics is tied to the same initial condition uncertainty, namely, the magnitude of the lower-tropospheric easterly winds along the Texas–Mexico border.

One way to validate the importance of the water vapor field along the Texas–New Mexico border at 1200 UTC is to compute forecast errors with respect to dropwindsonde data (UCAR/NCAR–Earth Observing Laboratory 2016) deployed during MPEX IOP 8 for each ensemble member, similar to what was done in Berman et al. (2017). In particular, the errors for the 10 members with the largest Texas Panhandle J_{VKE}, which have erroneously large convection, are compared to the 10 members with the smallest J_{VKE}, which are closer to reality (i.e., isolated convection in metric region). Moreover, if the regions identified by this technique are critical to the convection forecast, than the members with the smallest J_{VKE} should have statistically smaller errors in water vapor and meridional wind with respect to dropwindsondes in the sensitive regions compared to the members with the largest J_{VKE}. Here, the sensitive dropwindsondes are the five sondes east of 105°W and south of 36°N, which roughly enclose the region where J_{VKE} is most sensitive to the 1200 UTC 700–800-hPa water vapor mixing ratio (cf. Fig. 9 for sensitive region and Fig. 1g for drop

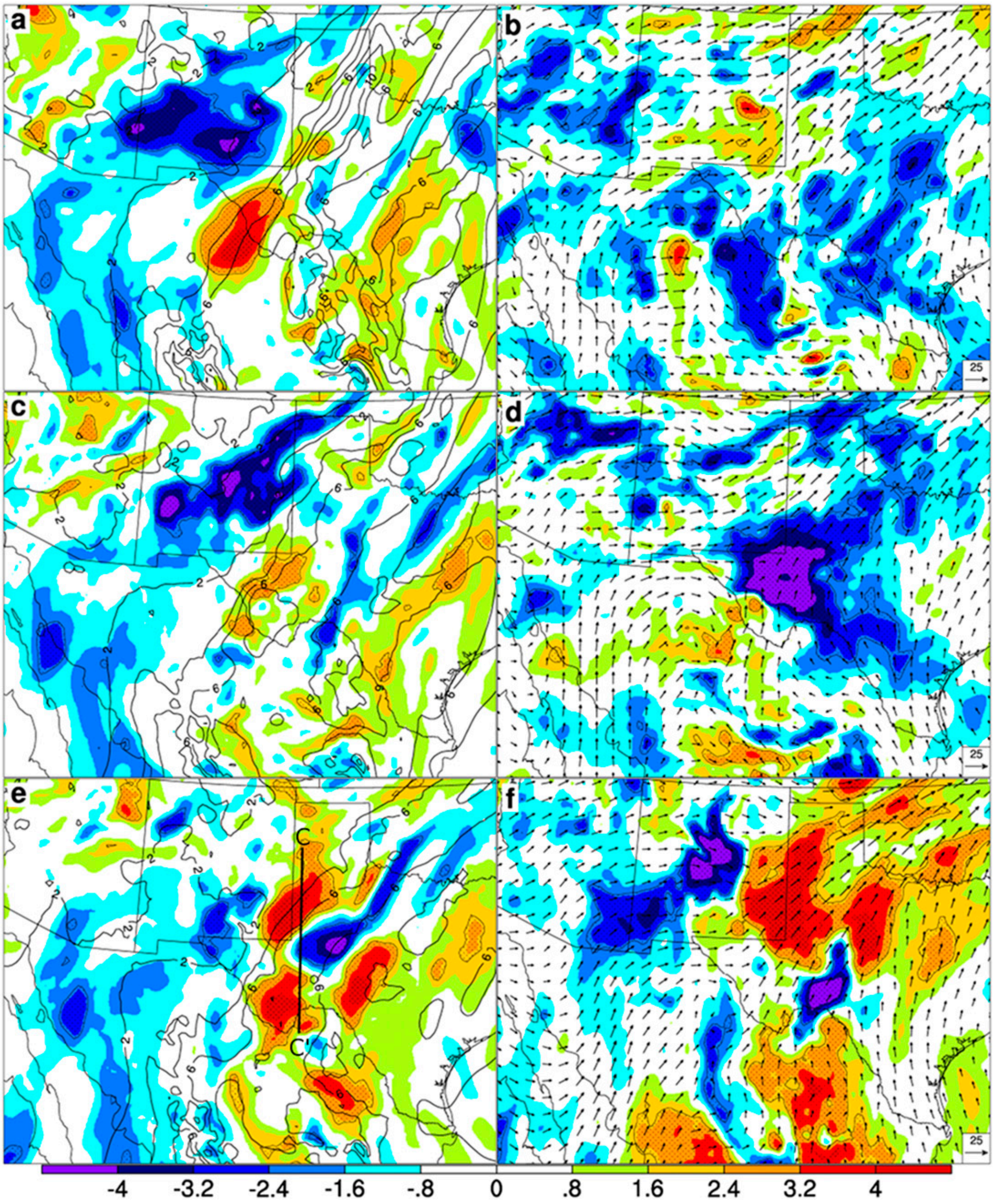

FIG. 12. Sensitivity of the 5–8-h maximum vertical kinetic energy averaged over the box shown in Fig. 11b to the 0-h 700–800-hPa (a) integrated water vapor and (b) zonal wind (color shading, $m^2 s^{-2}$) initialized at 0000 UTC 28 May 2013. Stippled regions indicate where the sensitivity is statistically significant at the 95% confidence level. The contours and vectors are the ensemble-mean values ($kg\ m^{-2}$ and $m\ s^{-1}$, respectively). (c),(d) As in (a),(b), but for the 6-h forecast. (e) As in (a), but for the 12-h forecast. (f) As in (b), but for the 12-h meridional wind forecast. The black line in (e) denotes the location of the cross section for Fig. 13.

locations). The dropwindsondes were deployed between 1200 and 1400 UTC; therefore, in order to capture the evolution of forecast fields, the model forecast data are temporally interpolated to the dropwindsonde release time.

As might be expected, the members with small J_{VKE} are characterized by smaller errors with respect to these dropwindsondes. To compare different levels and sets of dropwindsondes, normalized errors are shown, which is defined as the difference between the small and large J_{VKE} member errors, divided by the ensemble-mean error. Figure 14 indicates that the members with small J_{VKE} have specific humidity errors between 600 and

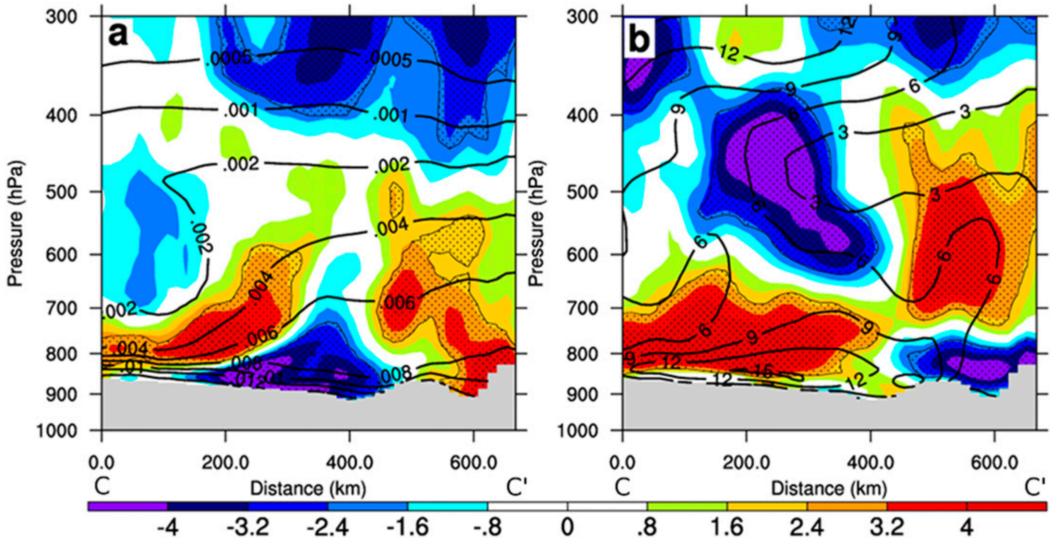

FIG. 13. Sensitivity of the 5–8-h maximum vertical kinetic energy averaged over the metric region shown in Fig. 11b to the 12-h (a) water vapor mixing ratio and (b) meridional wind along the cross section shown in Fig. 12e (color shading, $m^2 s^{-2}$) initialized at 0000 UTC 28 May 2013. Stippled regions indicate where the sensitivity is statistically significant at the 95% confidence level. The contours are the ensemble-mean fields [$kg\,kg^{-1}$ and $m\,s^{-1}$ in (a),(b), respectively].

800 hPa that are between 40% and 80% lower than large J_{VKE} members, which suggests that the small J_{VKE} members are producing better convective forecasts because they are characterized by a more accurate upstream water vapor forecast within the sensitive region. Furthermore, the error difference between the small and large J_{VKE} members is below 20% when considering all dropwindsondes, suggesting that the small J_{VKE} members have a better forecast because they are more accurate in the sensitive region and not more accurate over the entire region over which dropwindsondes were deployed (mainly Colorado and New Mexico). The meridional wind error differences are also consistent with the specific humidity differences, such that the small J_{VKE} members have between 40% and 60% lower errors in the sensitive region over the same vertical

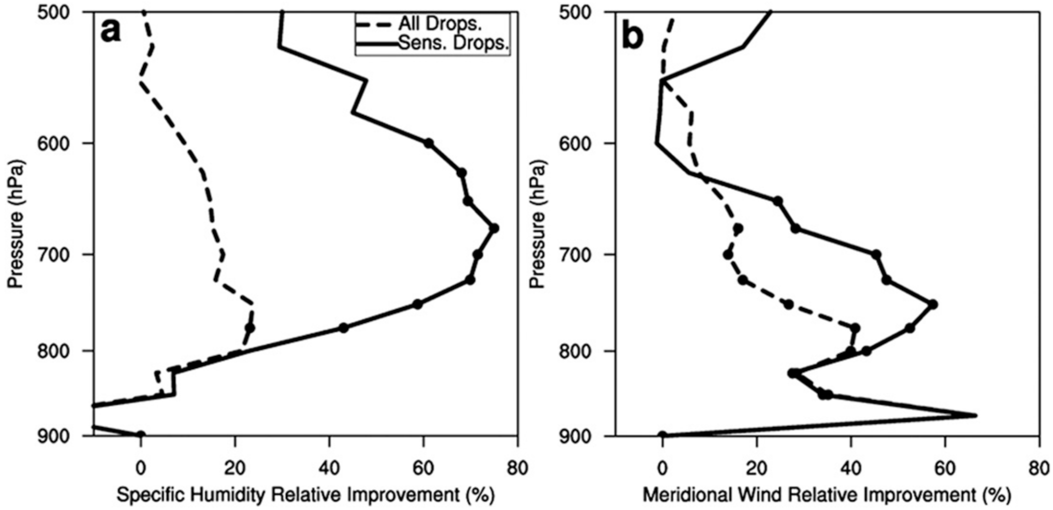

FIG. 14. Relative difference in (a) specific humidity and (b) meridional wind mean-absolute error between the weak and strong members with respect to dropwindsondes in the sensitive region (black) and all dropsondes (dashed) initialized at 0000 UTC 28 May 2013. The distribution of dropwindsondes is shown in Fig. 1g. Levels with a black circle denote where the difference is statistically significant at the 95% confidence level.

layer, with smaller differences overall when considering all dropwindsondes (Fig. 14b).

Another method of confirming the importance of uncertainty in the 0-h water vapor mixing ratio along the dryline is to perturb the initial conditions within the sensitive region and observe the resulting change in the forecast convection later that day in a manner similar to what was done in previous studies (e.g., Torn and Hakim 2009; Torn and Cook 2013). Perturbed initial conditions for individual ensemble members are generated via

$$x^p_{i,n} = x^a_{i,n} + \frac{\partial x^a_i}{\partial J_{\mathrm{sens}}}\alpha, \qquad (2)$$

where

$$\frac{\partial x^a_i}{\partial J_{\mathrm{sens}}} = \frac{\mathrm{cov}(\mathbf{J}_{\mathrm{sens}}, \mathbf{x}^a_i)}{\mathrm{var}(\mathbf{J}_{\mathrm{sens}})},$$

$\mathbf{x}^a_i$ is the $1 \times M$ ensemble estimate of the ith control analysis state variable, n refers to the ensemble member, $\mathbf{J}_{\mathrm{sens}}$ is the $1 \times M$ ensemble estimate of the 0-h 700–800-hPa water vapor mixing ratio averaged over the maximum sensitive region along the dryline (the statistically significant sensitivity region along the Texas–Mexico border seen in Fig. 10a), and α is the perturbation amplitude being applied to J_{sens}. This initial condition perturbation equation is essentially like assimilating an observation of J_{sens} with a specified innovation of α and an observation error variance of 0. Rather than integrating all 50 perturbed forecasts forward, only two members of the ensemble are used in these experiments (other members exhibit similar behavior; not shown). Recall that member 28 was characterized by low J_{VKE}. As a consequence, applying an $\alpha > 0$ initial condition perturbation (i.e., increasing the water vapor in the sensitive region) should result in larger J_{VKE} for this member if J_{VKE} is sensitive to the water vapor in this location. Moreover, member 33 was characterized by high J_{VKE}; therefore, applying an $\alpha < 0$ initial condition perturbation (i.e., decreasing the water vapor in the sensitive region) should result in smaller J_{VKE} for this member. A range of α values are tested, though only $\alpha = 1.64\,\mathrm{kg\,m^{-2}}$ is shown here, which is the mean difference in J_{sens} between the 10 members with the largest J_{VKE} and the 10 members with the smallest J_{VKE}.

The evolution of water vapor differences indicates an asymmetric response to positive or negative initial condition changes within the sensitive region. Figure 15a shows the control and perturbation 0-h 700–800-hPa water vapor for member 33 (a member with large J_{VKE}), assuming $\alpha = -1.64\,\mathrm{kg\,m^{-2}}$. For this member, the initial condition difference is maximized along the dryline in far west Texas, with differences up to $2.1\,\mathrm{kg\,m^{-2}}$; this region coincides with the sensitive region identified for J_{q_v}. By 12 h (Fig. 15c), the differences exceed $2.5\,\mathrm{kg\,m^{-2}}$ and are maximized along the dryline along Texas–New Mexico border, close to the sensitive region identified previously (cf. Fig. 9c). At 18 h (just prior to CI), much of the Texas Panhandle is characterized by negative 700–800-hPa integrated water vapor differences in excess of $2.5\,\mathrm{kg\,m^{-2}}$ (Fig. 15e), and large regions where the MLCIN is $40\,\mathrm{J\,kg^{-1}}$ greater than the control (not shown), which helps to suppress convection. By contrast, applying an $\alpha = 1.64\,\mathrm{kg\,m^{-2}}$ to member 28 (a small J_{VKE} member) does not produce a similar response in the 700–800-hPa integrated water vapor in the Texas Panhandle prior to CI. While the 0-h difference is identical, but opposite signed to the perturbation applied to member 33 (Fig. 15b), the differences between the control and perturbed initial condition experiment for member 28 are not as extensive as for member 33 at 12 h (Fig. 15d) or 18 h (Fig. 15f), such that only a small area has a difference that exceeds $2.5\,\mathrm{kg\,m^{-2}}$. In particular, the 18-h differences in 700–800-hPa water vapor and MLCIN have mainly passed by the forecast metric area at 1800 UTC, such that the largest differences are along the Texas–Oklahoma border. This result suggests that it is easier to obtain a longer-lasting drying of the members with extensive convection by perturbing the initial conditions within the sensitive region, compared to trying to moisten the lower troposphere for a member with less convection; other members have qualitatively similar results (not shown).

The asymmetric response to the water vapor perturbations also extends to the convective evolution over the Texas Panhandle. Perturbing member 33 leads to significantly less convection within the forecast metric area, both in terms of the simulated radar reflectivity (cf. Figs. 16a and 3e) and J_{VKE} ($56.5\,\mathrm{m^2\,s^{-2}}$ in the control, $3.4\,\mathrm{m^2\,s^{-2}}$ in the perturbed experiment). By contrast, perturbed member 28 still exhibits minimal convection along this part of the dryline during this period (cf. Figs. 16b and 3f); therefore, it appears that perturbing the initial conditions to reduce the water vapor can reduce the amount of convection within the sensitive region. By contrast, adding water vapor to a member with little convection appears to have minimal impact. It is unclear why this asymmetric response exists, though it may be related to how these initial condition perturbations impact the far west Texas convection early in the forecast. Perturbed member 33 exhibits significantly less convection at 6 h, which is at least partially related to having weaker upslope flow at 0 h, and hence there is less outflow to modify the dryline position to the north. By contrast, perturbed member 28 has a similar distribution of west Texas convection and cold pool

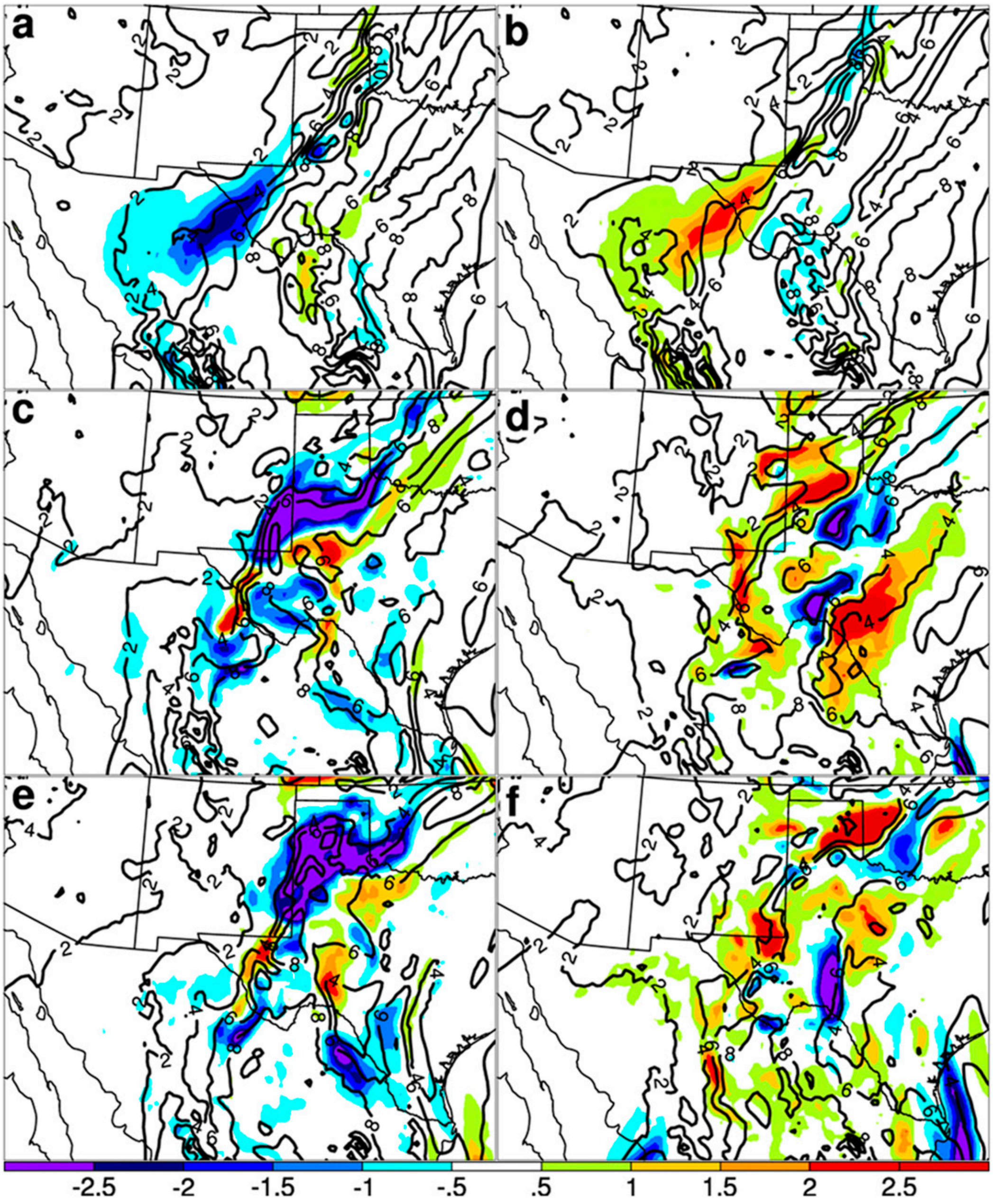

FIG. 15. (a) Difference between the perturbed initial condition and control member 33 (a) 0-, (c) 12-, and (e) 18-h 700–800-hPa integrated water vapor (color shading, kg m^{-2}) for the forecast initialized at 0000 UTC 28 May 2013. The contours denote the control forecast values. (b),(d),(f) As in (a),(c),(e), but for member 28.

activity during the first 6 h, despite having stronger upslope flow (not shown).

6. Summary and conclusions

This study explores the sensitivity of convection forecasts along the dryline during two consecutive days characterized by weak synoptic forcing during the MPEX field program. The forecast sensitivities are evaluated by applying the ensemble-based sensitivity method to WRF ensemble forecasts of these events initialized at 0000 UTC. Here, the strength of convection is measured via the vertical kinetic energy forecasts averaged over objectively defined forecast metric boxes that encompass the regions of largest convection forecast uncertainty close to the time of CI.

During both 27 and 28 May, the spatial extent of convection is a strong function of the moisture above the

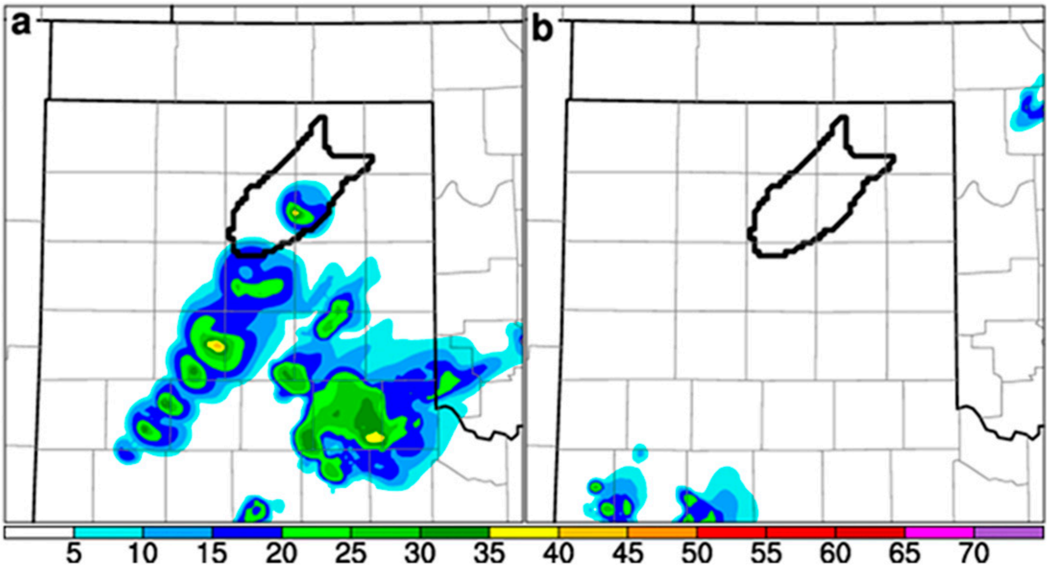

FIG. 16. The 21-h simulated radar reflectivity forecast for perturbed initial condition ensemble members (a) 33 and (b) 28 initialized at 0000 UTC 28 May 2013. The outlined area in (b) and (c) denotes the forecast metric region used in the sensitivity calculations.

boundary layer, generally between 700 and 800 hPa. As a consequence, the members with greater convection are characterized by smaller CIN within the region of interest and in turn larger maximum vertical motion values, which limited CI from taking place. This result is at least qualitatively consistent with the idealized results of James and Markowski (2010), who found that lower moisture above the boundary layer limits convective motions. In this situation, the weaker convective motion would make it more difficult for near-surface parcels to overcome the inhibition present on this day, particularly given there is no synoptic or mesoscale feature that could otherwise help CI. On both days, the convection forecasts along the dryline are sensitive to the lower-tropospheric water vapor farther south along the dryline at earlier times, such that shifting the dryline position to the west is associated with greater water vapor and hence more extensive convection. By contrast, both days exhibit minimal sensitivity to mid- and upper-tropospheric features at earlier times.

This sensitive region becomes more difficult to trace backward in time beyond 0600 UTC, which is likely related to a number of factors, including non-Gaussian distribution of forecast metric values, and having higher topography to the south. One way to overcome the former is to employ a forecast metric that measures the average integrated water vapor averaged over the convection forecast metric region since the amount of water vapor moisture in this region appears to distinguish between members with large and small convection. The water vapor metric is also sensitive to the water vapor along the dryline; the sensitive region can be traced further backward in time. For both cases, the water vapor is sensitive to the amount of easterly flow along the Texas–New Mexico border. For 27 May, this wind is tied to uncertainty in a weak PV anomaly initially over central Mexico, while for 28 May the sensitivity to the wind does not appear to be tied to any particular subsynoptic feature. This easterly wind helps to increase the water vapor advection along the dryline. Moreover, the water vapor along the dryline on 28 May appears to exhibit a complex relationship with convection that forms along the Texas–New Mexico border around 0600 UTC, such that increasing the lower-tropospheric moisture and easterly flow is associated with more overnight convection, leading to the creation of cold pools that subsequently modulate the dryline position.

Verification of individual ensemble members against MPEX dropwindsonde observations within the sensitive region and perturbed initial condition experiments confirm the importance of uncertainty in the water vapor field along the dryline on 28 May. The members with less convection, which were closer to reality, have statistically lower water vapor errors with respect to dropwindsondes in the sensitive region 8 h prior to CI. Moreover, perturbing the initial conditions in a manner that decreases the water vapor within the sensitive region can suppress convection for the members that produce excessive convection; however, adding water vapor in the sensitive region does not lead to more extensive convection for those members that lacked convection in the control.

The results for this study have some intriguing implications for CI forecasts along the dryline during days without any clear feature to focus CI. Similar to previous sensitivity studies, convective forecasts appear to be sensitive to thermodynamic fields and boundaries; however, unlike these previous studies, the position of these boundaries does not appear to be tied to the position of larger-scale synoptic features that might be expected to modulate the environment (e.g., Bednarczyk and Ancell 2015; Torn and Romine 2015; Berman et al. 2017; Hill et al. 2016). Moreover, these convective forecasts appear to be most sensitive to the water vapor above the boundary layer; however, the results here suggest that the evolution of water vapor is not merely the advection of initial condition uncertainty. For 28 May, there was a complex interaction with overnight convection, which subsequently modifies the dryline position. These results argue for additional observations of water vapor above the boundary layer, particularly for those cases where a larger-scale feature is not present.

Acknowledgments. This paper benefited from discussions with Morris Weisman (NCAR). Real-time observation data access was provided by MADIS, COSMIC, and SSEC. We would like to acknowledge high-performance computing support from Yellowstone (ark:/85065/d7wd3xhc) provided by NCAR's Computational and Information Systems Laboratory, sponsored by the National Science Foundation. This work was supported by NSF Grant 1239787 and NOAA Award NA14OAR4830172.

REFERENCES

Anderson, J., 2001: An ensemble adjustment Kalman filter for data assimilation. *Mon. Wea. Rev.*, **129**, 2884–2903, doi:10.1175/1520-0493(2001)129<2884:AEAKFF>2.0.CO;2.

——, T. Hoar, K. Raeder, H. Liu, N. Collins, R. Torn, and A. Arellano, 2009: The Data Assimilation Research Testbed: A community data assimilation facility. *Bull. Amer. Meteor. Soc.*, **90**, 1283–1296, doi:10.1175/2009BAMS2618.1.

Barker, D. M., and Coauthors, 2012: The Weather Research and Forecasting Model's Community Variational/Ensemble Data Assimilation System: WRFDA. *Bull. Amer. Meteor. Soc.*, **93**, 831–843, doi:10.1175/BAMS-D-11-00167.1.

Bednarczyk, C. N., and B. C. Ancell, 2015: Ensemble sensitivity analysis applied to a Southern Great Plains convective event. *Mon. Wea. Rev.*, **143**, 230–249, doi:10.1175/MWR-D-13-00321.1.

Bei, N., and F. Zhang, 2007: Impacts of initial condition errors on mesoscale predictability of heavy precipitation along the Mei-Yu front of China. *Quart. J. Roy. Meteor. Soc.*, **133**, 83–99, doi:10.1002/qj.20.

Berman, J. D., R. D. Torn, G. S. Romine, and M. Weisman, 2017: Sensitivity of Northern Great Plains convection forecasts to upstream and downstream forecast errors. *Mon. Wea. Rev.*, doi:10.1175/MWR-D-16-0353.1, in press.

Coniglio, M. C., D. J. Stensrud, and L. J. Wicker, 2006: Effects of upper-level shear on the structure and maintenance of strong quasi-linear mesoscale convective systems. *J. Atmos. Sci.*, **63**, 1231–1252, doi:10.1175/JAS3681.1.

Durran, D. R., and M. Gingrich, 2014: Atmospheric predictability: Why butterflies are not of practical importance. *J. Atmos. Sci.*, **71**, 2476–2488, doi:10.1175/JAS-D-14-0007.1.

——, and J. A. Weyn, 2016: Thunderstorms do not get butterflies. *Bull. Amer. Meteor. Soc.*, **97**, 237–243, doi:10.1175/BAMS-D-15-00070.1.

——, P. A. Reineck, and J. D. Doyle, 2013: Large-scale errors and mesoscale predictability in Pacific Northwest snowstorms. *J. Atmos. Sci.*, **70**, 1470–1487, doi:10.1175/JAS-D-12-0202.1.

Ek, M. B., K. E. Mitchell, Y. Lin, E. Rodgers, P. Grunmann, V. Koren, G. Gayno, and J. D. Tarpley, 2003: Implementation of Noah land surface model advances in the National Centers for Environmental Prediction operational mesoscale Eta model. *J. Geophys. Res.*, **108**, 8851, doi:10.1029/2002JD003296.

Errico, R. M., K. D. Raeder, and L. Fillion, 2003: Examination of the sensitivity of forecast precipitation rates to possible perturbations of initial conditions. *Tellus*, **55A**, 88–105, doi:10.1034/j.1600-0870.2003.201394.x.

Gilmore, M. S., and L. J. Wicker, 1998: The influence of midtropospheric dryness on supercell morphology and evolution. *Mon. Wea. Rev.*, **126**, 943–958, doi:10.1175/1520-0493(1998)126<0943:TIOMDO>2.0.CO;2.

Hill, A. J., C. C. Weiss, and B. C. Ancell, 2016: Ensemble sensitivity analysis for mesoscale forecasts of dryline convection initiation. *Mon. Wea. Rev.*, **144**, 4161–4182, doi:10.1175/MWR-D-15-0338.1.

Hohenegger, C., and C. Schar, 2007: Predictability and error growth dynamics in cloud-resolving models. *J. Atmos. Sci.*, **64**, 4467–4478, doi:10.1175/2007JAS2143.1.

Iacono, M. J., J. S. Delamere, E. J. Mlawer, M. W. Shephard, S. A. Clough, and W. D. Collins, 2008: Radiative forcing by long-lived greenhouse gases: Calculations with the AER radiative transfer models. *J. Geophys. Res.*, **113**, D13103, doi:10.1029/2008JD009944.

James, R. P., and P. M. Markowski, 2010: A numerical investigation of the effects of dry air aloft on deep convection. *Mon. Wea. Rev.*, **138**, 140–161, doi:10.1175/2009MWR3018.1.

——, ——, and J. M. Fritsch, 2006: Bow echo sensitivity to ambient moisture and cold pool strength. *Mon. Wea. Rev.*, **134**, 950–964, doi:10.1175/MWR3109.1.

Janjić, Z. I., 1994: The step-mountain eta coordinate model: Further developments of the convection, viscous sublayer, and turbulence closure schemes. *Mon. Wea. Rev.*, **122**, 927–945, doi:10.1175/1520-0493(1994)122<0927:TSMECM>2.0.CO;2.

——, 2001: Nonsingular implementation of the Mellor–Yamada level 2.5 scheme in the NCEP Meso model. Tech. Rep. NCEP Office Note 437, National Centers for Environmental Prediction, Camp Springs, MD, 61 pp.

Kirkpatrick, C., E. W. McCaul, and C. Cohen, 2009: Variability of updraft and downdraft characteristics in a large parameter space study of convective storms. *Mon. Wea. Rev.*, **137**, 1550–1561, doi:10.1175/2008MWR2703.1.

——, ——, and ——, 2011: Sensitivities of simulated convective storms to environmental CAPE. *Mon. Wea. Rev.*, **139**, 3514–3532, doi:10.1175/2011MWR3631.1.

Kursinski, E. R., G. A. Hajj, J. T. Shofield, R. P. Linfied, and K. R. Hardy, 1997: Observing Earth's atmosphere with radio occultation measurements using the Global Positioning

System. *J. Geophys. Res.*, **102**, 23 429–23 465, doi:10.1029/97JD01569.

Lorenz, E. N., 1969: The predictability of a flow which possesses many scales of motion. *Tellus*, **21A**, 289–307, doi:10.3402/tellusa.v21i3.10086.

Martin, W. J., and M. Xue, 2006: Sensitivity analysis of convection of the 24 May 2002 IHOP case using very large ensembles. *Mon. Wea. Rev.*, **134**, 192–207, doi:10.1175/MWR3061.1.

McCaul, E. W., C. Cohen, and C. Kirkpatrick, 2005: The sensitivity of simulated storm structure, intensity, and precipitation efficiency to environmental temperature. *Mon. Wea. Rev.*, **133**, 3015–3037, doi:10.1175/MWR3015.1.

Melhauser, C., and F. Zhang, 2012: Practical and intrinsic predictability of severe and convective weather at the mesoscales. *J. Atmos. Sci.*, **69**, 3350–3371, doi:10.1175/JAS-D-11-0315.1.

Mellor, G. L., and T. Yamada, 1982: Development of a turbulence closure model for geophysical fluid problems. *Rev. Geophys. Space Phys.*, **20**, 851–875, doi:10.1029/RG020i004p00851.

Mlawer, E. J., S. J. Taubman, P. D. Brown, M. J. Iacono, and S. A. Clough, 1997: Radiative transfer for inhomogeneous atmosphere: RRTM, a validated correlated-k model for the long-wave. *J. Geophys. Res.*, **102**, 16 663–16 682, doi:10.1029/97JD00237.

Nuss, W. A., and D. K. Miller, 2001: Mesoscale predictability under various synoptic regimes. *Nonlinear Processes Geophys.*, **8**, 429–438, doi:10.5194/npg-8-429-2001.

Richardson, Y. P., K. K. Droegenmeier, and R. P. Davies-Jones, 2007: The influence of horizontal environmental variability on numerically simulated convective storms. Part I: Variations in vertical shear. *Mon. Wea. Rev.*, **135**, 3429–3455, doi:10.1175/MWR3463.1.

Romine, G. S., C. S. Schwartz, C. Snyder, J. L. Anderson, and M. L. Weisman, 2013: Model bias in a continuously cycled assimilation system and its influence on convection-permitting forecasts. *Mon. Wea. Rev.*, **141**, 1263–1284, doi:10.1175/MWR-D-12-00112.1.

——, ——, R. D. Torn, and M. L. Weisman, 2016: Impact of assimilating dropsonde observations from MPEX on ensemble forecasts of severe weather events. *Mon. Wea. Rev.*, **144**, 3799–3823, doi:10.1175/MWR-D-15-0407.1.

Schumacher, R. S., 2015: Sensitivity of precipitation accumulation in elevated convective systems to small changes in low-level moisture. *J. Atmos. Sci.*, **72**, 2507–2524, doi:10.1175/JAS-D-14-0389.1.

Schwartz, C. S., G. S. Romine, M. L. Weisman, R. A. Sobash, K. R. Fossell, K. W. Manning, and S. B. Trier, 2015: A real-time convection-allowing ensemble prediction system initialized by mesoscale ensemble Kalman filter analyses. *Wea. Forecasting*, **30**, 1158–1181, doi:10.1175/WAF-D-15-0013.1.

Skamarock, W. C., and M. L. Weisman, 2009: The impact of positive-definite moisture transport on NWP precipitation forecasts. *Mon. Wea. Rev.*, **137**, 488–494, doi:10.1175/2008MWR2583.1.

——, and Coauthors, 2008: A description of the Advanced Research WRF version 3. NCAR Tech. Note NCAR/TN-475+STR, 113 pp., doi:10.5065/D68S4MVH.

Tegen, I., P. Hollrig, M. Chin, I. Fung, D. Jacob, and J. Penner, 1997: Contribution of different aerosol species to the global aerosol extinction optical thickness: Estimates from model results. *J. Geophys. Res.*, **102**, 23 895–23 915, doi:10.1029/97JD01864.

Thompson, G., P. R. Field, R. M. Rasmussen, and W. D. Hall, 2008: Explicit forecasts of winter precipitation using an improved bulk microphysics scheme. Part II: Implementation of a new snow parameterization. *Mon. Wea. Rev.*, **136**, 5095–5115, doi:10.1175/2008MWR2387.1.

Tiedtke, M., 1989: A comprehensive mass flux scheme for cumulus parameterization in large-scale models. *Mon. Wea. Rev.*, **117**, 1779–1800, doi:10.1175/1520-0493(1989)117<1779:ACMFSF>2.0.CO;2.

Torn, R. D., and G. J. Hakim, 2008: Ensemble-based sensitivity analysis. *Mon. Wea. Rev.*, **136**, 663–677, doi:10.1175/2007MWR2132.1.

——, and ——, 2009: Initial condition sensitivity of western Pacific extratropical transitions determined using ensemble-based sensitivity analysis. *Mon. Wea. Rev.*, **137**, 3388–3406, doi:10.1175/2009MWR2879.1.

——, and D. Cook, 2013: The role of vortex and environment errors in Hurricanes Danielle and Karl (2010) genesis forecasts. *Mon. Wea. Rev.*, **141**, 232–251, doi:10.1175/MWR-D-12-00086.1.

——, and G. S. Romine, 2015: Sensitivity of Central Oklahoma convection forecasts to upstream potential vorticity anomalies during two strongly forced cases during MPEX. *Mon. Wea. Rev.*, **143**, 4064–4087, doi:10.1175/MWR-D-15-0085.1.

——, G. J. Hakim, and C. Snyder, 2006: Boundary conditions for limited-area ensemble Kalman filters. *Mon. Wea. Rev.*, **134**, 2490–2502, doi:10.1175/MWR3187.1.

UCAR/NCAR–Earth Observing Laboratory, 2016: NSF/NCAR G-V dropsonde high resolution data, version 3.0. UCAR/NCAR–Earth Observing Laboratory, accessed 26 August 2016, doi:10.5065/D6ZS2TP6.

Velden, C., and Coauthors, 2005: Recent innovations in deriving tropospheric winds from meteorological satellites. *Bull. Amer. Meteor. Soc.*, **86**, 205–223, doi:10.1175/BAMS-86-2-205.

Wandishin, M. S., D. J. Stensrud, S. L. Mullen, and L. J. Wicker, 2008: On the predictability of mesoscale convective systems: Two-dimensional simulations. *Wea. Forecasting*, **23**, 773–785, doi:10.1175/2008WAF2007057.1.

Weisman, M. L., C. Davis, W. Wang, K. W. Manning, and J. B. Klemp, 2008: Experiences with 0–-36-h explicit convective forecasts with the WRF-ARW Model. *Wea. Forecasting*, **23**, 407–437, doi:10.1175/2007WAF2007005.1.

——, and Coauthors, 2015: The Mesoscale Predictability Experiment (MPEX). *Bull. Amer. Meteor. Soc.*, **96**, 2127–2149, doi:10.1175/BAMS-D-13-00281.1.

Zhang, C., Y. Wang, and K. Hamilton, 2011: Improved representation of boundary layer clouds over the Southeast Pacific in WRF-ARW using a modified Tiedtke cumulus parameterization scheme. *Mon. Wea. Rev.*, **139**, 3489–3513, doi:10.1175/MWR-D-10-05091.1.

Zhang, F., C. Snyder, and R. Rotunno, 2003: Effects of moist convection on mesoscale predictability. *J. Atmos. Sci.*, **60**, 1173–1185, doi:10.1175/1520-0469(2003)060<1173:EOMCOM>2.0.CO;2.

——, Z. Meng, and A. Aksoy, 2006: Test of an ensemble Kalman filter for mesoscale and regional-scale data assimilation. Part I: Perfect model experiments. *Mon. Wea. Rev.*, **134**, 722–736, doi:10.1175/MWR3101.1.